The experimental plan for cryogenic layered target implosions on the National Ignition Facility—The inertial confinement approach to fusion

M. J. Edwards,[1] J. D. Lindl,[1] B. K. Spears,[1] S. V. Weber,[1] L. J. Atherton,[1] D. L. Bleuel,[1] D. K. Bradley,[1] D. A. Callahan,[1] C. J. Cerjan,[1] D Clark,[1] G. W. Collins,[1] J. E. Fair,[1] R. J. Fortner,[1] S. H. Glenzer,[1] S. W. Haan,[1] B. A. Hammel,[1] A. V. Hamza,[1] S. P. Hatchett,[1] N. Izumi,[1] B. Jacoby,[1] O. S. Jones,[1] J. A. Koch,[1] B. J. Kozioziemski,[1] O. L. Landen,[1] R. Lerche,[1] B. J. MacGowan,[1] A. J. MacKinnon,[1] E. R. Mapoles,[1] M. M. Marinak,[1] M. Moran,[1] E. I. Moses,[1] D. H. Munro,[1] D. H. Schneider,[1] S. M. Sepke,[1] D. A. Shaughnessy,[1] P. T. Springer,[1] R. Tommasini,[1] L. Bernstein,[1] W. Stoeffl,[1] R. Betti,[2] T. R. Boehly,[2] T. C. Sangster,[2] V. Yu. Glebov,[2] P. W. McKenty,[2] S. P. Regan,[2] D. H. Edgell,[2] J. P. Knauer,[2] C. Stoeckl,[2] D. R. Harding,[2] S. Batha,[3] G. Grim,[3] H. W. Herrmann,[3] G. Kyrala,[3] M. Wilke,[3] D. C. Wilson,[3] J. Frenje,[4] R. Petrasso,[4] K. Moreno,[4] H. Huang,[4] K. C. Chen,[5] E. Giraldez,[5] J. D. Kilkenny,[5] M. Mauldin,[5] N. Hein,[5] M. Hoppe,[5] A. Nikroo,[5] and R. J. Leeper[6]

[1]*Lawrence Livermore National Laboratory, Livermore, California 94550, USA*
[2]*Laboratory for Laser Energetics, University of Rochester, Rochester, New York 14623, USA*
[3]*Los Alamos National Laboratory, Los Alamos, New Mexico 87545, USA*
[4]*Plasma Fusion and Science Center, Massachusetts Institute of Science and Technology, Cambridge, Massachusetts 02139, USA*
[5]*General Atomics, San Diego, California 92121, USA*
[6]*Sandia National Laboratory, Sandia, New Mexico 87185, USA*

(Received 31 August 2010; accepted 8 March 2011; published online 1 June 2011)

Ignition requires precisely controlled, high convergence implosions to assemble a dense shell of deuterium-tritium (DT) fuel with $\rho R > \sim 1$ g/cm^2 surrounding a 10 keV hot spot with $\rho R \sim 0.3$ g/cm^2. A working definition of ignition has been a yield of ~1 MJ. At this yield the α-particle energy deposited in the fuel would have been ~200 kJ, which is already $\sim 10\times$ more than the kinetic energy of a typical implosion. The National Ignition Campaign includes low yield implosions with dudded fuel layers to study and optimize the hydrodynamic assembly of the fuel in a diagnostics rich environment. The fuel is a mixture of tritium-hydrogen-deuterium (THD) with a density equivalent to DT. The fraction of D can be adjusted to control the neutron yield. Yields of $\sim 10^{14-15}$ 14 MeV (primary) neutrons are adequate to diagnose the hot spot as well as the dense fuel properties via down scattering of the primary neutrons. X-ray imaging diagnostics can function in this low yield environment providing additional information about the assembled fuel either by imaging the photons emitted by the hot central plasma, or by active probing of the dense shell by a separate high energy short pulse flash. The planned use of these targets and diagnostics to assess and optimize the assembly of the fuel and how this relates to the predicted performance of DT targets is described. It is found that a good predictor of DT target performance is the THD measurable parameter, Experimental Ignition Threshold Factor, ITFX $\sim Y \times$ dsf $^{2.3}$, where Y is the measured neutron yield between 13 and 15 MeV, and dsf is the down scattered neutron fraction defined as the ratio of neutrons between 10 and 12 MeV and those between 13 and 15 MeV. © *2011 American Institute of Physics*. [doi:10.1063/1.3592173]

I. INTRODUCTION

The goal of the National Ignition Campaign[1] (NIC) on the National Ignition Facility[2] (NIF) is to use an indirectly driven spherical implosion to assemble and ignite a mass of DT fuel. In order to do this, the fuel must be assembled into a dense shell ~1000 g/cc, surrounding a lower density hot spot.[3–5] Ignition is approached as the hot spot central temperature reaches a temperature ~10–12 keV and a ρR ~0.3 g/cm^2, approximately equivalent to an α-particle stopping range. Ignition will occur if the total ρR of the imploded fuel is $> \sim 1$ g/cm^2, so that the hot spot is confined long enough for the temperature to bootstrap by α-heating to several tens of keV.

Achieving these ρR and T conditions requires a low adiabat (low entropy), high convergence ~30–40 spherical implosion. This demands precise control over the laser pulse and target which have been carefully designed to balance optimally the key implosion parameters of velocity (v), adiabat (α), hot spot shape (s), and ablator fuel mix (m). These key implosion parameters and their role in optimizing the ignition point design are discussed extensively in the companion paper on the point design in this issue.[6] These can be considered to be implosion input parameters that control the output variables ρR and T, and are discussed further in Sec. IV. Because of uncertainties in the underlying physics, as well as approximations in the numerical models used to design the target, it cannot be guaranteed, *a priori*, that the

specified laser pulse and target will produce the desired v, α, *s*, *m* and hence the ρR and *T* necessary for ignition. For this reason, the NIC includes a series of experiments, which are designed to *tune* the laser pulse and target parameters to obtain the desired conditions. This tuning campaign is discussed extensively in a companion paper in this issue.[7] The tuning campaign uses ignition targets modified to measure experimental observables, which relate to the key implosion parameters. While the uncertainty in optimum laser pulse and target will be substantially reduced after these experiments, some offset from optimal will still exist because of small surrogacy errors between the tuning target and ignition targets, and because of experimental uncertainties. Furthermore, none of the initial tuning targets will include a cryogenic fuel layer. Because of this, physics phenomena associated with this layer, specifically mix of material at the ablator-ice interface, and hot spot formation inside the low adiabat main fuel will remain untested experimentally in the tuning campaign.

Once the tuning experiments have advanced, the next step will be to introduce cryogenic layered targets. Capsules with DT layers produce extremely harsh and challenging environments, typically upwards of $\sim 10^{16}$ neutrons ($\sim$30 kJ) even when they perform poorly. This results in significant facility impacts and severely limits diagnostics options. Therefore, to study and optimize layered target performance and fuel assembly in a diagnostics rich environment, capsules with "dudded" fuel layers have been introduced into the experimental plan. The fuel consists primarily of tritium ($\sim$75%) and hydrogen ($\sim$25%), with a trace of D ($\sim$2–10%). The precise fuel proportions are selected to preserve the mass and particle density of the layer, making these capsules essentially hydrodynamically equivalent to DT ignition targets up to the point that α-heating becomes important. Extensive numerical simulation shows that the performance of the dudded "THD" (tritium-hydrogen-deuterium) target is a good predictor of the yield of an identical twin DT target. The key is determining the combinations of experimental observables from the THD targets that furnish an accurate prediction of the DT yield. Particularly important parameters are found to be the THD neutron yield, *Y*, relating to the mass and temperature of the hot spot, and the fraction of 14 MeV neutrons scattered by the surrounding fuel, dsf (down scattered fraction), which is related to the total ρR. It is found that $Y \times \mathrm{dsf}^{2.3}$, (Ref. 8) which turns out to be equivalent to a Lawson criterion for ICF,[9,10] is a particularly good predictor of DT performance. Thus the THD implosions should measure how successful the tuning experiments have been and eliminate the surrogacy uncertainty to the level of the experimental errors. The prediction of DT performance from the THD results relies on the burn physics models used, in particular on calculations of alpha particle stopping and thermal conduction, which cannot be confirmed under the conditions of the compressed fuel until DT experiments are performed.

The amount of D in THD targets has been selected so that the neutron yield is such that both nuclear and x-ray diagnostics work well providing a wealth of complementary data on performance. For targets with $\sim$2% D, the yield is expected to be in the $\sim 1\text{–}3 \times 10^{14}$ ($\sim$300–1000 J) range, with $\sim$90% coming from DT reactions and most of the remainder from TT fusion. Only $\sim$20% of the fusion product energy is in α-particles and less than 50% is deposited into the hot spot, i.e. less than $\sim$30–100 J. These yields are small compared to the $\sim$10–15 kJ of kinetic energy of the imploding fuel and have no feedback on the hydrodynamics of the target, effectively separating the hydrodynamic assembly from α-heating and burn. This is a very important feature resulting in a controlled environment in which to study and optimize the fuel assembly with diagnostics signatures that vary smoothly and slowly as the THD performance spans the DT ignition cliff. Conversely, the yield of DT targets over this range can vary hugely with even small changes in the implosion conditions resulting in a very different hydrodynamic behavior and diagnostics signatures, making it more difficult to understand the experiments. An additional and not insignificant benefit is the relatively minimal impact of THD yields on the facility operations.

Following any laser and target adjustments to correct for surrogacy errors, and successful confirmation of fuel assembly using the THD targets, a DT target would be expected to ignite. The working definition for ignition on NIF is a yield equal to or greater than the input laser energy ($\sim$1–1.3 MJ for the current point design). This definition was adopted following an NAS review in 1996–1997. Although the design goals are typically $\sim$10–20 MJ on NIF, a yield of 1 MJ provides an unambiguous demonstration of ignition. In a typical ignition target, the imploding fuel has a kinetic energy of less than 20 kJ. With a MJ of yield, 200 kJ of alphas would be deposited into that fuel volume, over $10\times$ the energy provided directly by the implosion process. Without alpha deposition, the yield of the assembled DT with a 50/50 mixture would be only $\sim$10–20 kJ. It is the alpha deposition which heats the hot spot and generates a self-sustaining burn wave in the surrounding main fuel. In a typical NIF ignition target, this self-sustaining burn wave will be initiated when the central ion temperature reaches 10–12 keV. At that time, total yields are 100–200 kJ so that 20–40 kJ of alpha particles have been deposited in the fuel, several times the initial fuel kinetic energy. Beyond this time, the evolution of the burning fuel is dominated by alpha particle heating and the subsequent expansion which terminates the burn. In the discussion below, we will refer to "ignition time" in the DT targets as the time at which the central temperature reaches 12 keV. DT targets will produce very different diagnostics signatures compared to THD targets, making ignition unambiguous. The key signatures lie in the emitted neutron spectrum. First the total neutron yield increases by $\sim$2–3 orders of magnitude and the spectral width of the primary DT neutron peak becomes highly broadened[11] as a result of burn averaged ion temperatures $\sim$30 keV compared to $\sim$4 keV for THD. Added to this, the burn width shortens from $\sim$100 ps to $\sim$10 ps because of the very high pressures that are generated, and x-ray and neutron images of the implosion become $\sim 3\times$ larger due to the burn wave propagation into the surrounding fuel.

In this paper we discuss the role of layered target implosions on the path to ignition. The results presented derive

from multi-dimensional radiation hydrocode simulations and post processing thereof. The paper is arranged as follows. In Sec. II the targets are described. Section III addresses THD and DT implosion dynamics, similarities, and contrasts. Section IV discusses physics based performance metrics as well as the sensitivity of those metrics to the principal factors that influence the implosion. Section V addresses diagnostics signatures relating to those metrics, as well as presenting a brief overview of diagnostics. Section VI discusses the determination of target performance based on experimental observables in the presence of shot-to-shot variations. Section VII provides a summary.

II. TARGETS

The generic target that has been designed to achieve the ρR and T conditions necessary for ignition on NIF is shown in Fig. 1 (Ref. 4). Between ~1 and 1.8 MJ of 3ω (0.35 μm wavelength) laser light is focused into the cylindrical high Z, uranium, U, or Au hohlraum, ~ 10 mm in length and ~5 mm in diameter. The U hohlraum has a thin gold, Au, passivating layer. The 192 laser beams of NIF are grouped into 48 quads which enter the hohlraum through laser entrance holes (LEHs) which are ~50–60% the diameter of the hohlraum. They are arranged effectively into two cones from either end: an outer cone (44.5° and 50°) and an inner cone (23°, 30°). The quads are arranged on the inside of the hohlraum walls to form three rings of 16 quads each. The location and relative brightness of the rings are adjusted to obtain symmetric radiation drive.[12] The capsule has a low Z ablator (CH or Be) ~2 mm diameter and ~0.2 mm thick.[13,14] The THD or DT fuel is contained within the capsule in the form of a solid cryogenic layer ~0.07 mm thick with density of 0.25 g/cc at a temperature ~18.3 K, 1.5° below the triple point.[15,16] The precise temperature depends on the layer composition and is set, so that the central vapor density is ~0.3 mg/cc. This parameter is a strong lever on the final pressure achievable because it sets the amplitude of the initial back pressure that slows the implosion during stagnation. The ignition point design and the basis for the details which define it are discussed in detail in a companion paper[6] in this issue.

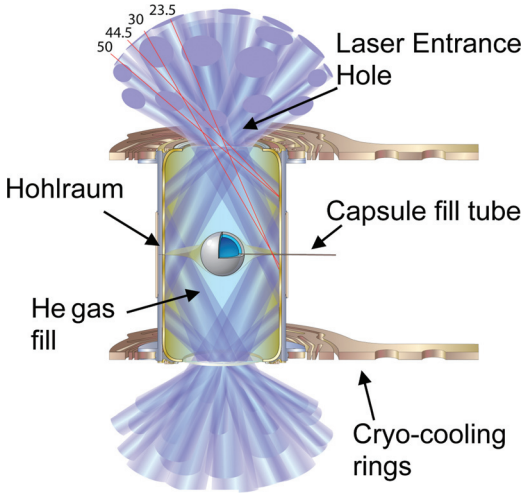

FIG. 1. (Color) Schematic of NIF ignition target. The hohlraum is made of uranium with a thin passivating layer of gold ~0.5 μm thick on the inside surface. It is filled with He gas at a density ~0.96 mg/cc, which controls wall motion for drive symmetry control. The dimensions have been selected based on recent NIF experiments to obtain symmetric implosions. (For a more complete description see Ref. 6).

The THD capsule is essentially the same as that ignition capsule except the 50:50 DT fuel is replaced by a dudded, deuterium poor mixture. The capsule details are shown schematically in Fig. 2 and listed in Table I. A detailed description of this basic target design can be found elsewhere.[17] The ablator has the now familiar five-layer design[18] with the three internal layers doped with Ge in the style of an Olympic podium. These layers are designed to optimize the tradeoff between implosion velocity and hydrodynamic instability growth at the fuel/ablator interface by moderating preheating of the ablator next to the fuel by energetic x-rays from the hohlruam drive.[6]

In order to keep the hydrodynamics of the ice layer equivalent to that of a DT target, the density of the ice layer is kept the same as DT ice. This is achieved by keeping the average atomic number of the THD ice the same as 50:50 DT, i.e., 2.5, which makes the density of the THD layer the same as that of DT ~0.25g/cc. This constraint can be written as

$$f_H = 1/2(1/2 - f_D)$$
$$f_T = 1/2(3/2 - f_D),$$

where the f's are the number fractions of H, D, and T, respectively.

III. THD AND DT IMPLOSIONS

In this section, we provide an overview of the indirect drive target dynamics together with some explanation of the main parameters that control target performance and how these are set in experiments. This is important to understand the role of the layered target experiments in optimizing performance. The discussion approximately follows the "build-a-pulse" philosophy adopted by the tuning experiments.

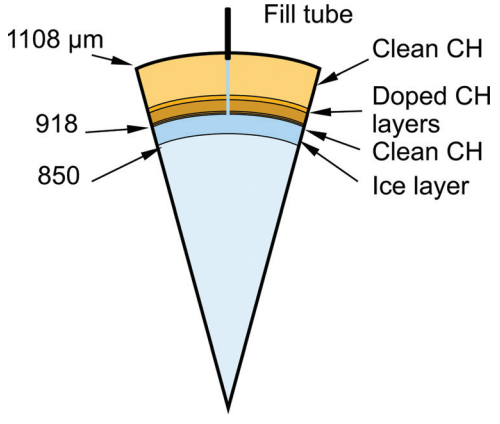

FIG. 2. (Color) Schematic of NIF CH ignition capsule. The capsule ablator has five layers, three of which are doped with Ge to control hydrodynamic instability at the ablator-ice interface. Heating of the inner clean CH layer by x-rays >1.8 keV, which pass through the ice drives a Rayleigh-Taylor unstable configuration at the interface. The amount of Ge is set to control the Atwood number such that instability growth is acceptable. The details of the design attempt to optimize the overall efficiency while controlling instability. (For a more complete description see Ref. 6).

TABLE I. Capsule properties.

Component	ΔR (μm)	%Ge	ρ (g/cc)	Mass (mg)
Outer clean layer	133	0.0	1.069	1.94
1st doped layer	13	0.5	1.108	0.17
2nd doped layer	34	1.0	1.147	0.44
3rd doped layer	5	0.5	1.108	0.06
Inner clean layer	5	0.0	1.069	0.06
Total ablator	190			2.66
Ice layer	68		0.255	0.17
Central gas[a]	850		0.296 mg/cc	772 ng

[a]The central gas density depends on the fuel composition as well as the fielding temperature. The above values are for a fielding temperature of 17.4 K, 1.5 K below the triple point, for a central gas composition of H:D:T 0.92:0.0078:0.072, which corresponds to a fuel layer composition of H:D:T 24:2:74.

A thorough and detailed discussion of target design and tuning experiments can be found in two companion articles in this issue[6,7] and in earlier review papers.[4]

The implosion begins as the laser light enters the hohlraum. It is converted with a high efficiency (~80–90%)[19] in the Au to x-rays which heat the hohlraum creating an almost thermal radiation bath with a temperature ~250–300 eV depending on the design. The thermal x-rays ablate the low-Z capsule, generating a rocket like thrust. The laser power is carefully shaped in time to produce a sequence of four shocks timed, so that they coalesce just inside the inner radius of the ice in order to keep the fuel nearly Fermi degenerate as the x-ray driven ablation pressure is gradually increased from an initial shock pressure of ~1 Mbar to its peak value of ~100 Mbar (Fig. 3). The shock strengths are set to predetermined values in the tuning experiments by adjusting the laser power levels. The pulse timings are adjusted to obtain the correct shock coalescence, which is a function of capsule thickness. Any change in thickness later in the campaign would require a new set of laser pulse timings set in new experiments.

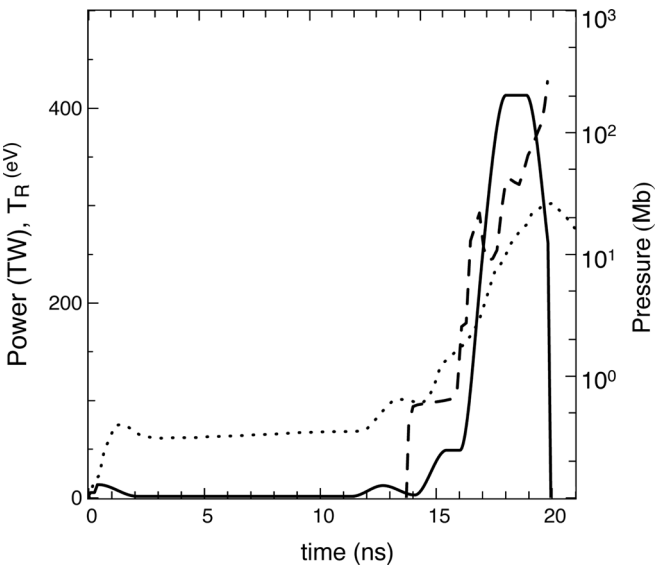

FIG. 3. Laser power (solid) simulated x-ray drive temperature in the hohlraum (dot) and pressure in the ice layer (dash) as a function of time. The laser power is stepped in time to gradually increase the x-ray drive on the capsule such that the pressure in the ice is increased in four shocks from ~1 Mbar to a value in excess of 100 Mbar during the implosion phase. The steps are timed such that the shocks coalesce just inside the ice layer which minimizes the entropy generation in the layer. The first shock enters the ice close to ~14 ns after it has traversed the ablator.

After passage of the 4th shock, the shell begins to accelerate inwards under the action of the ablative thrust, reaching a peak velocity in excess of ~350 km/s once the shell has shrunk to ~1/4 its original size. By this time, the DT has been compressed to ~25 g/cc and has a temperature of only ~10eV. The fuel continues to be shielded from the intense radiation field in the hohlraum by a thin layer of ablator material consisting of ~5–10% of the mass of the original shell, which is more than adequate for this function. The amount of unablated mass necessary is a function of the amount of instability growth.[6] There is a tradeoff between implosion velocity, which continues to increase as more mass is ablated, and the penetration of the fuel by bubbles from hydrodynamic instability growth in the ablator. The tuning experiments may need to adjust both the thickness of the capsule and peak laser power to obtain the desired velocity, at the same time as meeting the unablated mass requirement.[7]

During the subsequent few hundred picoseconds following peak velocity, the capsule decelerates, drawing on its kinetic energy to compress most of the fuel into a high density shell. The hot spot mass (and ρR_{HS}) grows in time as a subsonic electron thermal conduction wave eats into the surrounding fuel. Once the central temperature reaches ~4–5 keV, α-particle heating of the hot spot begins to become important in a DT target. Until this point the development of DT and THD implosions is expected to be nearly equivalent and is predicted to be so in numerical simulations (see Fig. 4). The subsequent progress of the THD and DT implosion is now contrasted. For this purpose we have selected 1D and 2D simulations of a high performing DT target and companion THD target (see Table II for following discussion). In a 1D THD implosion about 30% of the kinetic energy ($KE_{max\ TOT}$) is used to heat a hot spot (E_{HS}) that naturally forms at the center of the implosion, and there is little kinetic energy (KE_{hyd} ~1%) left in the fuel at stagnation (equivalent to peak x-ray brightness). The hot spot mass (M_{HS}) is ~8% of the initial fuel mass. In 2D, with instability growth from ablator and ice roughness, the hot spot energy is reduced to a little more than 20% because the clean volume is reduced due to instability growth at the cold fuel hot spot interface. This is reflected in the mass of the 2D hot spot which is ~70% of that in 1D, or ~5.5% of the initial fuel mass. An additional consequence of the instability in a THD implosion is that there is ~15% of the energy left in the fuel kinetic energy at peak x-ray brightness. The above ratios are similar in a DT target except the hot spot energy at ignition time is ~200% of the maximum incoming kinetic energy, and the mass and ρR of the hot spot (ρR_{HS}) are ~2 × that of the THD target at stagnation. This can be attributed almost entirely to α-heating.

In a THD target, there is little additional heating provided above the PdV work of the imploding shell. As the stagnation process progresses the ρR_{HS} of the hot spot continues to increase reaching ~0.3 g/cm^2 at peak x-ray emission.

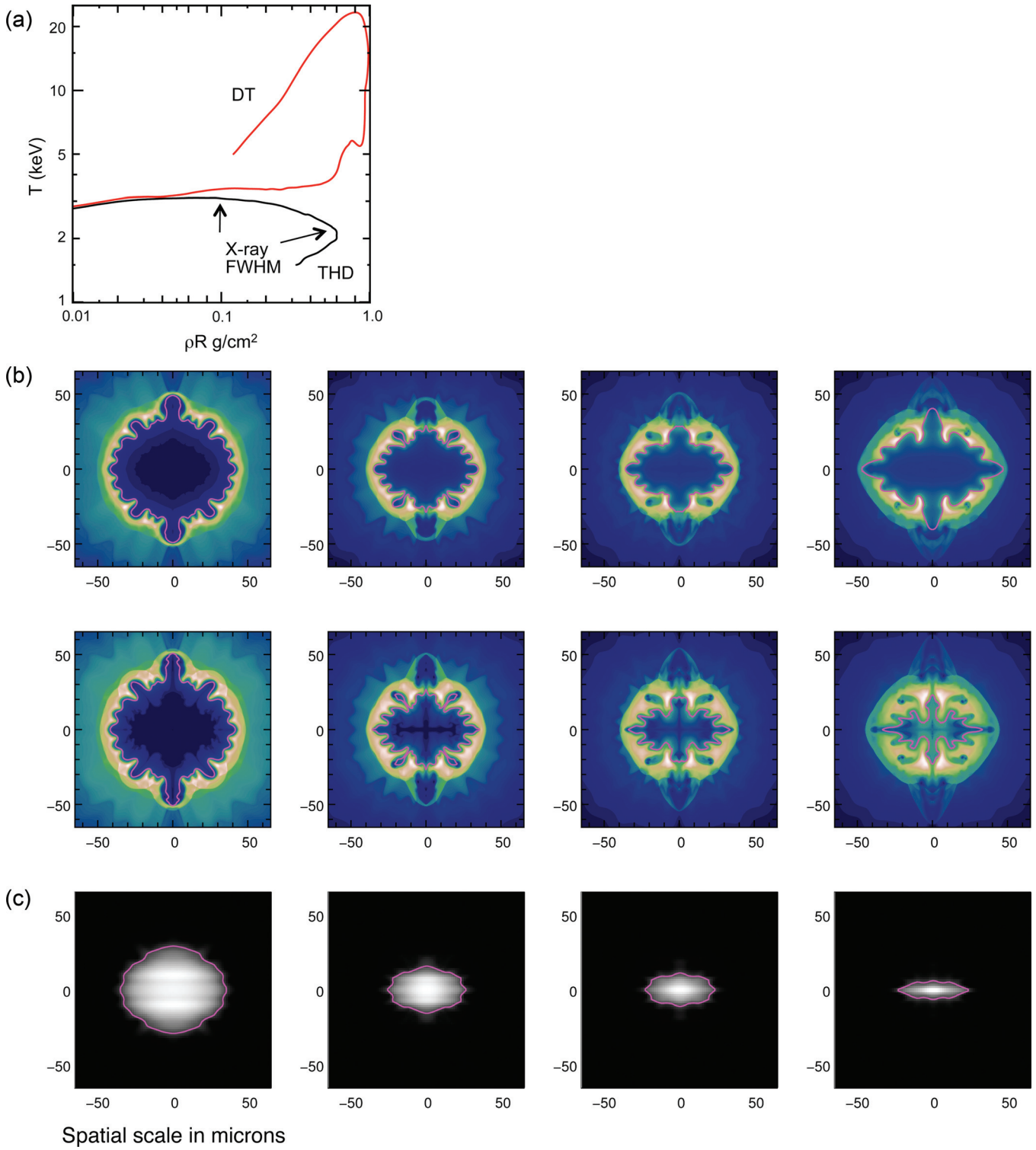

FIG. 4. (a) (Color) Predicted trajectory of equivalent THD and DT (red) implosions in the hot spot ρR, T plane. The implosions are essentially identical until the average temperature in the hot spot reaches ~3 keV at which time self heating due to α-particle deposition in the DT target begins to become energetically important. The segment of the THD trajectory representing the period of FWHM of x-ray and neutron emission is also shown. (b). (Color) Time sequence (21.19, 21.25, 21.28, 21.32) ns of simulated density fields from 2D simulations, producing the data in 4(a) roughly 40 ps apart. Prior to significant α-heating the THD (lower sequence) and DT (upper sequence) targets look very similar. Once α-heating becomes significant in the DT fuel, the spikes of ice at the hot/cold fuel interface seen in the THD implosion are ablated and the back pressure is enough to halt the implosion by ignition time. In contrast, the hot spot in the THD target continues to shrink as the cooler ice fingers continue to fall towards the center. (c). (Color) Time sequence from a simulated THD implosion of x-ray images filtered for >10 keV, which are very close to the actual hot spot size and low mode shape. As the implosion progresses, the hot spot shrinks as Rayleigh-Taylor instability continues to cause fingers of cold fuel to penetrate ever further into the hot core. The images used 10 μm and 30 ps temporal and spatial resolution, respectively.

The fuel in the hot spot then cools and shrinks causing its ρR to continue to increase reaching a peak value ~ 0.6 g/cm^2 after which the fuel disassembles. The boundary of the hot spot is defined as the contour which is at less than half the maximum density and at temperature >1 keV. This entire process takes ~100 ps. In contrast, self heating by α-deposition in a DT hot spot results in a strikingly different behavior as is evident in Figs. 4(b) and 4(c). As the temperature continues to rise in a DT target, the heat wave is driven ever further into the surrounding fuel, providing significant ablative stabilization of Rayleigh-Taylor growth at the surface of the hot spot. Much of the mass of the fingers of cold ice falling into the hot spot is effectively burned off by α-deposition and electron thermal conduction becoming part of the hot spot as a result. In contrast in a THD target, the fingers continue to fall into and shrink the much cooler hot spot. After successful hydrodynamic assembly, this nuclear, or α-heating phase, is the critical step leading to ignition. Once ignition occurs, ~50 ps earlier than peak x-ray brightness in an equivalent THD target (Fig. 5), a burn wave propagates out through the entire fuel so the ρR of the "hot spot" grows to encompass the total fuel ρR. This is illustrated in Fig. 4a.

In ICF, ignition is determined by the point at which alpha deposition is sufficient to initiate a self-sustaining burn wave into the surrounding cold fuel. As stated above, this occurs once the central temperature of the hot spot reaches ~10–12 keV and its ρR_{HS} reaches at least ~0.3 g/cm^2, approximately the stopping range of the 3.5 MeV α-particle at ~10 keV. At ignition time the hot spot in a NIF ignition target contains ~10% of the total DT mass and has a density and radius ~100 g/cc and ~35 μm, respectively. In the absence of α-deposition, the hot spot would be less massive with a radius of ~25 μm. The surrounding relatively cold fuel is ~10 μm thick and has an average density in excess of ~1000 g/cc. Once the burn wave is initiated, it propagates until it runs out of fuel. The fuel in an ICF implosion is confined only by its inertia. It continues to burn until the dense shell containing most of the fuel blows itself apart on the time scale of the order of a sound wave crossing time ~10 ps. The thermonuclear yield depends on the amount of fuel burned up during this time. For approximately spherical assemblies and for average temperatures of ~30 keV that would be typical of a NIF target, the burn up fraction can be estimated by the well known expression.[4]

$$f_{burnup} = \frac{\rho R}{\rho R + 6},$$

where $\rho R = \rho R_{\mathrm{Total}}$, the total ρR in g/cm^2 of the assembly including any remaining ablator material. On the NIF, the peak ρR is ~2.25 g/cm^2 (see Table II) so the burn up fraction is ~25%. The energy released is given by

$$E_{DT} = 3.4 \times 10^{11} f_B M_g \mathrm{J},$$

where M_g is the mass of fuel in grams. For the point design target parameters given in Table II, the fuel mass is ~0.17 mg corresponding to a nominal yield ~15 MJ or $\sim 5 \times 10^{18}$ neutrons. TableII shows that the nominal 1D point design has a calculated yield somewhat more than this, while the typical 2D calculation had somewhat lower yield. A detailed discussion of the expected point design performance is given in Ref. 6.

The THD hot spot shape at peak x-ray brightness is a good surrogate for the DT target at ignition time, although the radius is only expected to be ~25 μm for the THD target compared to ~35 μm for the DT target. The exact radius will

TABLE II. Physics properties and observables of THD and DT implosions.

Physics	DT	THD(2%)	DT 1D	THD(2%) 1D
E_{absorbed} (kJ)	160	160	160	160
V_{imp} (km/s)	365.0	364.9	368.7	368.3
$KE_{\mathrm{max\ TOT}}$ (kJ)	16	16	16	16
$KE_{\mathrm{max\ fuel}}$ (kJ)	11.32	11.33	11.55	11.53
KE_{hyd} (kJ)	3.93	2.25	0.56	0.27
E_{HS}(kJ)	29.5	3.28	24.3	4.66
E_{fuel}(kJ)	16.9	10.85	16.1	10.18
M_{HS} (μg)	22.5	9.36	30.3	13.8
F_{HS}	0.132	0.055	0.178	0.081
ρR_{HS} (g/cm^2)	0.67	0.36	0.60	0.42
ρR_{Fuel} (g/cm^2)	0.93	1.41	1.03	1.46
ρR_{TOT} (g/cm^2)	2.28	2.31	2.23	2.48
$<\rho R_{\mathrm{TOT}}>$ (g/cm^2)	1.38	2.31	1.35	2.23
R_{HS} (μm)	32.4	20.7	29.6	22.3
Observables				
Y	11.35 MJ	600 J	18.2 MJ	1187 J
Y_n	4.0e18	2.1e14	6.5e18	4.2e14
$Y_{\mathrm{X>10keV}}$	163 kJ	10 J	140 kJ	18 J
$Y_{\mathrm{X>25keV}}$	64 kJ	1.9 J	46 kJ	3.8 J
$<T_{\mathrm{ion}}>$ (keV)	26.5	3.29	37.3	3.02
P_0 (μm)$_{\mathrm{X>10keV}}$	24.0	20.5	23.2	21.2
DSF	0.07	0.075	0.08	0.085
t_{burn} (ps)	18.2	78.0	24.9	94.1
t_{bang} (ns)	21.36	21.28	21.33	21.30

E_{absorbed}: capsule absorbed energy.
V_{imp}: maximum implosion velocity of the fuel defined as $V_{imp} = Max\sqrt{\int_{fuel} V^2 dm \Big/ 2M_{fuel}}$.
$KE_{\mathrm{max\ TOT}}$: maximum kinetic energy of the fuel and unablated ablator on implosion.
$KE_{\mathrm{max\ fuel}}$: maximum kinetic energy of the fuel on implosion.
KE_{hyd}: kinetic energy of the fuel at ignition (DT) or bang time (THD).
E_{HS}: hot spot thermal energy at ignition (DT) or bang time (THD).
E_{fuel}: thermal energy in dense fuel shell (i.e., not including hot spot)
M_{HS}: hot spot mass at ignition (DT) or bang time (THD).
F_{HS}: hot spot mass expressed as fraction of initial fuel mass.
ρR_{HS}: hot spot ρR at ignition (DT) or bang time (THD).
ρR_{Fuel}: fuel ρR at ignition (DT) or bang time (THD).
ρR_{TOT}: total (fuel + ablator) ρR at ignition (DT) or bang time (THD).
$\langle \rho R_{\mathrm{TOT}} \rangle$: burn averaged total ρR.
R_{HS}: hot spot radius defined as 50% fuel density < 1 keV.
Y: total energy produced by DT, DD, TT reactions.
Y_{n}: total number of neutrons produced by DT, DD, TT reactions.
$Y_{\mathrm{X>10\ keV}}$: x-ray yield >10 keV photon energy.
$Y_{\mathrm{X>25\ keV}}$: x-ray yield >25 keV photon energy.
$\langle T_{\mathrm{ion}} \rangle$: burn averaged ion temperature.
$P_{0\mathrm{X>10\ keV}}$: average radius of 17% contour of hot spot x-ray image >10 keV photons.
DSF: down scattered neutron fraction defined as number of neutrons emitted from the capsule between 10 and 12 MeV to those emitted between 13 and 15 MeV.
t_{burn}: x-ray burn width; FWHM of emission >10 keV.
t_{bang}: time of peak x-ray brightness (x-ray bang time) >10 keV.

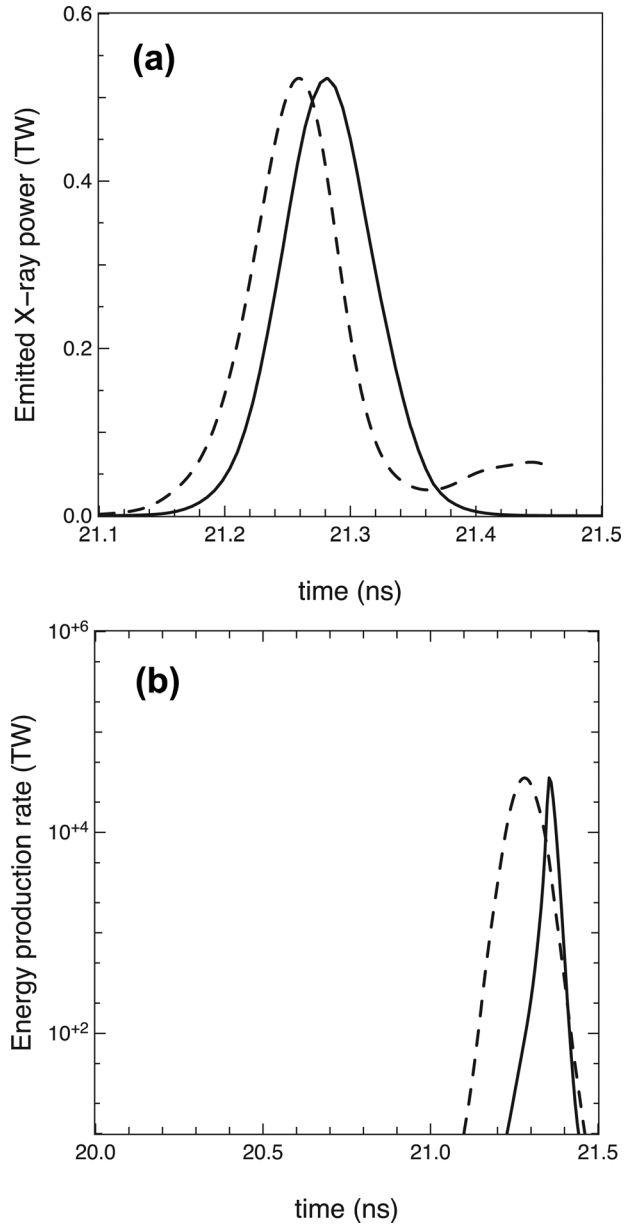

FIG. 5. (a) X-ray power (solid) emitted from the THD implosion simulation shown in Fig. 4 vs. time. The peak x-ray emission occurs very close to the peak thermonuclear energy production rate, shown by the dashed line normalized to the x-ray production rate. (b) Energy production rates in simulations of THD (dashed line) and the equivalent igniting DT target (solid line). The energy production rate indicated is for the DT ignition target. The peak energy production rate for the THD target has been normalized to that for the DT target to make it easier to compare the shape and timing of the burn history in the two targets. In this particular case, peak energy production rate in the DT occurs slightly later (~80 ps) than that in the dudded target. This is largely due to the additional time it takes for the hot spot formation process to advance in the run up to ignition.

depend on the amount of instability growth as well as on the seed, the main source of which is expected to be ice roughness (see Sec. VI).

In a THD target, the yield comes only from the hot spot generated by PdV work with negligible alpha heating. The mass and temperature of the hot spot are moderated by thermal conduction and its clean volume is limited by the growth of perturbations between ice and hot spot. The total ρR and stagnation pressure dictate the confinement time for the burn. The THD target yield depends on all these factors,[10] as well as on the composition of the fuel.

The deuterium fraction provides a mechanism to control the neutron yield to optimize diagnostics performance. The DT neutron yield in the THD target is proportional to $f_D f_T \sim 3/2 f_D - f_D^2$ which is proportional to f_D to the first order for the relatively D starved fuel for the THD targets. The yield from a series of 1D simulations is shown in Fig. 6 as a function of deuterium fraction in the fuel. The rate at which the yield increases is slightly faster than f_D. This is because there is a small amount of α-particle heating in the hot spot, which increases the hot spot temperature as f_D increases. Boot strap heating begins to strongly impact target evolution above ~25% D in these 1D simulations.

In practice the yields will be lower than these 1D values for two reasons. The first is because the central gas in the capsule prior to the laser shot is relatively hydrogen rich because of the higher vapor pressure of hydrogen relative to tritium.[16] For example for the case in which the ice composition is H:D:T 24:2:74, the gas composition will be H:D:T 0.92:0.0078:0.072. This has the effect of reducing the reactivity of the central gas significantly. Although the gas constitutes only a fraction ~10% of the mass of the final hot spot, 1 and 2D simulations indicate a yield reduction of ~40% due to this effect alone for an ice layer with 2% D. This is probably an upper limit on the yield reduction because the 2D simulations likely underestimate the degree of mixing between the hydrogen rich initial gas and ice that later becomes hot spot. This mixing will reduce the impact of the initial gas composition on the yield. It should be noted

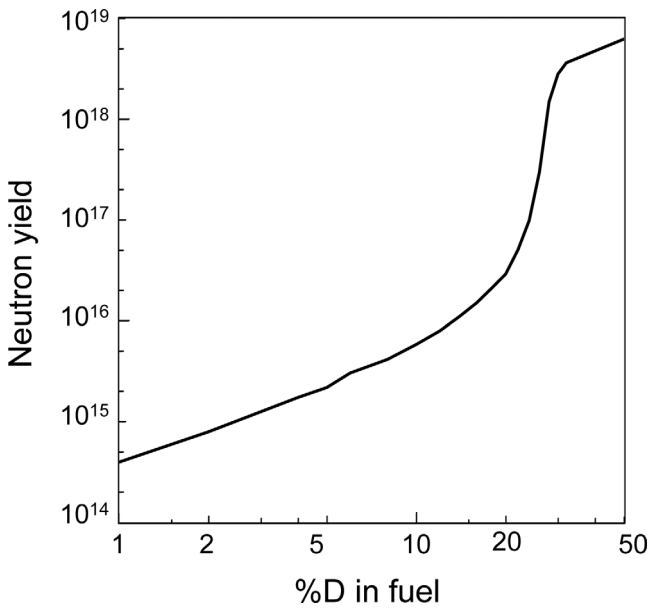

FIG. 6. Simulated 1D clean yield and burn averaged temperature as a function of %D in hydro-equivalent THD targets. The temperature increases with the fraction of deuterium because of a small amount of α-particle heating. As a result the yield increases slightly faster than linear in deuterium fraction. The central gas composition has been assumed to be the same as that of the ice rather than the more hydrogen rich composition that would be expected in order to provide an upper limit. The effect of the depletion of D and T in the initial central gas region, for the case of only 2% D fraction which consequently has a large hydrogen level in the central gas, is calculated to decrease these yields by ~40%.

that this effect becomes progressively less important as the fraction of hydrogen is reduced, and is unimportant in DT capsules.

The second effect reducing the yield from 1D is the growth of 3D hydrodynamic instability at the interface between the hot spot and ice, which reduces the clean volume of the hot spot as discussed above. As a result, for a well tuned THD target, the yield is expected to be ~0.45 the 1D clean value. For a well tuned target, the above two effects result in expected yields ~25% of those shown in Fig. 6.

IV. IMPLOSION PERFORMANCE

Achieving the ρR and T conditions necessary for ignition requires careful control of four key "input" parameters which characterize the expected target performance. These are velocity (v), fuel adiabat (α) or entropy, hot spot shape (s), and ablator fuel mix (m). It has been shown that these four parameters can be combined into an ignition threshold factor (ITF) that is a good predictor of DT yield.[6,20] The ITF is the ratio of the shell kinetic energy to the minimum required for ignition. It is normalized to unity when the gain is unity, i.e., for marginal ignition, and varies smoothly across the ignition cliff.

$$\mathrm{ITF} = I_0 \left(\frac{M_{DT}}{M_0}\right)\left(\frac{\mathrm{v}}{\mathrm{v}_0}\right)^8 \left(\frac{\alpha}{\alpha_0}\right)^{-4} \left(1 - 1.2\frac{\Delta R^{K-wtd}_{hotspot}}{R_{hotspot}}\right)^4 \left(\frac{M_{clean}}{M_{DT}}\right)^{0.5} (1 - P_{HS}).$$

The meaning of each term is explained in detail in Ref. 6, see also Fig. 7. Briefly, I_0 is the ITF of the baseline 1D system, which is typically ~3–5. M_{DT} is the mass of the fuel, while M_{clean} is the mass of fuel that remains free of ablator mix at the fuel/ablator interface. Subscript "0" refers to nominal values expected for a point design meeting requirements following the ignition optimization campaign. The peak implosion velocity is v and α is the fuel adiabat defined as the ratio of the fuel pressure compared to the minimum possible pressure from our detailed equation of state for DT

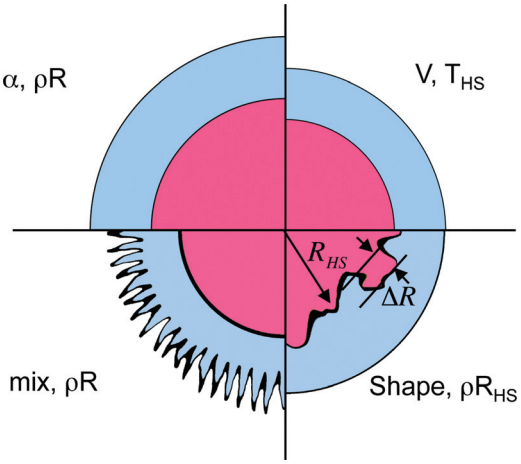

FIG. 7. (Color) Schematic showing how the four input implosion parameters for ITF (mix, velocity, adiabat, shape) relate to the outputs ρR and T.

when the fuel reaches 1000 g/cc. This minimum is close to the Fermi pressure for a degenerate electron gas. Both the velocity and adiabat are those for an equivalent 1D implosion in which the 3D effects which cause mix and perturb shape are absent. The expected values of v and α (i.e., v_o and α_o) after a successful experimental optimization campaign are ~370 km/s and 1.4, respectively. The 3D effects are included in the $\Delta R_{\mathrm{hotspot}}/R_{\mathrm{hotspot}}$ and the $M_{\mathrm{Clean}}/M_{\mathrm{DT}}$ terms. The former is the hot spot RMS fractional deviation from ideal 1D and includes a weighting, which slightly de-emphasizes the effect of low modes (<6) on the hot spot shape.[21] The nominal value of $\Delta R_{\mathrm{hotspot}}/R_{\mathrm{hotspot}}$ is ~0.15, so that ITF is reduced by a factor of about 0.5. The $M_{\mathrm{Clean}}/M_{\mathrm{DT}}$ term describes ablator-ice mix and is the fraction of ice that remains unmixed (containing <5% ablator by mass). The nominal value of $M_{\mathrm{Clean}}/M_{\mathrm{DT}}$ is ~0.7, reducing ITF by a factor ~0.85. The $(1\text{-}P_{hs})$ term is a measure of the impurities which have entered the hot spot, either from T decay which produces He, or from small amounts of mix which have penetrated the entire thickness of the cryo-fuel layer and entered the hot spot. This mix can come from the fill tube or from other isolated defects. The ITF parameters are not entirely uncoupled, and the point design target and laser pulse have been specified to optimally balance them. In particular as previously mentioned, there is a tension between the desire to achieve high implosion velocity ($\mathrm{ITF} \sim \mathrm{v}^8$) and the need to shield the capsule from the damaging effects of mix ($1\text{-}P_{\mathrm{HS}}$), which grow rapidly once perturbations become large enough to penetrate the ablator material into the hot spot.[22] There is an uncertainty as to the optimal balance, and layered THD experiments will be used to help establish this.

A. Simulation model

The calculations on which these values are based come from ensembles of HYDRA or LASNEX calculations.[23] In this paper we discuss only the HYDRA code and results from it. These codes have gone through decades of verification and validation on a wide range of test problems and experiments of ever increasing precision and fidelity to the key physics issues of ICF. As a result of these tests, there is a substantial level of confidence that the codes can be used as a design tool for ignition targets and that the general features and specifications obtained for these targets will be close to those required for ignition. However, because of physics uncertainties in quantities such as the equation of state, opacities, and laser plasma interactions, we anticipate that the details of the laser pulse and target parameters will have to be adjusted in a tuning campaign so that the v, α, s, m goals are met. The relationship between v, α, s, m and ρR, T in "burn off" implosions such as THD is shown schematically in Fig. 7 and are elaborated on below. To do this, we use results extracted from the large 2D ensemble of hydra simulations. The simulations used in this study modeled the nominal CH target design described in Sec. II with a 2% D fraction in the fuel and included only the capsule. The x-ray source used to drive the capsule was taken from an integrated 2D hydra simulation that included both capsule and hohlraum driven by the laser pulse shown in Fig. 3. This integrated simulation used a non-

local thermodynamic equilibrium treatment for the atomic physics and treated the radiation transport in the implicit monte carlo approximation. This model reproduces recent NIF hohlraum experiments in the 500 kJ–1.3 MJ range, extremely well.[24] The x-ray drive from the hohlraum simulation was applied to the capsule only simulations using the multi-group diffusion approximation in such a way that the resultant 1D implosion characteristics match those from the integrated 2D hohlraum/capsule simulation. The opacities for the CH were calculated in LTE using the OPAL[25] code, and VISTA[26] was used for the Ge dopant opacity. The equations of state were tabulated and based on the Thomas-Fermi-Dirac approximation adjusted to match laboratory data where possible.[27] Most of the simulations were meshed over 90° with reflecting boundary conditions at the equator (90°) and rotational symmetry at the pole, so that only even modes could be modeled. The mesh contained 512 zones in the angular direction and ~400 in the radial direction resolving up to mode $\ell \sim 100$ with ~20 mesh points per mode.

In the 2D simulations a nominal surface roughness was applied to each surface similar to the detailed prescription in Ref. 6. The most important surfaces are the inside ice surface, the ice-ablator interface, and the outside of the ablator. Following Ref. 6 the surfaces can be described by first specifying the inner ablator surface as a sum of randomly phased spherical harmonic amplitudes R_{lm} given by (for $\ell > 12$)

$$\left|R_{lm}^{inner}\right| = 300/l^{2.3} + \frac{0.06}{\left[(l/70)^{0.6} + (l/1200)^{3.5}\right]}.$$

To this was added a thickness described by

$$\left|T_{lm}\right| = (10/l)^5 + \left\{\frac{0.12}{\left[(l/60)^{0.7} + (l/1200)^{3.5}\right]}\right\}$$

with random phases which then defined an outer ablator surface. The outer ice surface was assumed to conform to the inside surface of the ablator. The inner ice surface can be described according to the spherical harmonic amplitudes for $\ell > 4$,

$$\left|T_{lm}^{(ice)}\right| = 1.8/\left[l^{1.1} + (l/25)^2\right],$$

randomly phased relative to the ablator's inner surface. Modes 1–4 have a constant power of 0.16 $\mu\mathrm{m}^2$ for each mode. A detailed rationale for this prescription can be found in Ref. 6. These expressions define the surface requirements that are predicted to be acceptable for instability growth in ignition capsules. Typical good capsule surfaces have amplitudes that are ~50–100% of these. The inner ablator surface is extremely smooth and most of the instability in the 2D simulations is governed by the outer ablator surface and ice surface. In the 2D simulations each surface presented here has been approximated by cosine modes such that each surface is physically virtually identical to the surfaces described above with an equivalent RMS. This avoids larger physical amplitudes near the poles that can occur with the spherical harmonic description in 2D. As stated above, most calculations included only even modes (maintaining the surface RMS) because of the 90° symmetry used. The actual surfaces used in the single variable sensitivity studies discussed below are shown in Fig. 8.

The simulations are not adequately resolved to calculate mixing at the ice-ablator interface due to the growth of high modes ~1000 at that interface. In more detailed simulations under the nominal point design drive conditions, this mixing is predicted to be a small effect with only the outer ~20% of the ice mass becoming mixed with ablator. This is discussed extensively in Ref. 6. This increases the fuel adiabat very slightly and has minor impact on performance. Where this is an important consideration in the following sections, it is discussed further.

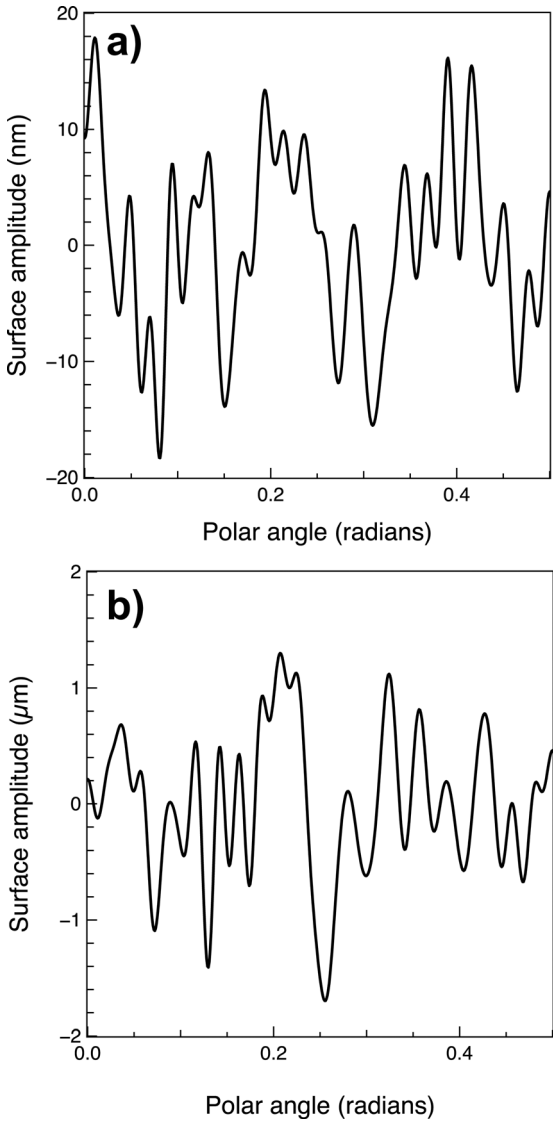

FIG. 8. (a) Amplitude of perturbation applied to the outer surface of the ablator in the 2D simulations reported in this article. This is composed of a sum of modes <100 with cosine amplitudes as defined in Sec. IV A. (b) Amplitude of perturbation applied to the inner ice surface in the 2D simulations reported in this article. This is composed of a sum of modes <100 with cosine amplitudes as defined in Sec. IV A.

B. Sensitivity of implosion parameters to implosion velocity and drive

For a given capsule design and underlying laser pulse shape, the implosion velocity is controlled primarily by the value of the peak drive. This is shown in Fig. 9(a) in which the maximum implosion velocity is plotted as a function of peak drive flux. The velocity is fit very well by $V_{imp} = 146ln(x) + 366\text{km/s}$, where x is the multiplier on the drive. The maximum implosion velocity here actually refers to the maximum fuel kinetic energy during the implosion phase and is defined as $V_{imp} = Max\sqrt{\int_{fuel} V^2 dm \Big/ 2M_{fuel}}$. The x-ray drive was adjusted relative to the baseline drive spectrum by applying a smooth multiplier (x-axis) across the peak. This would be achieved in practice by adjusting the peak laser power upon which the peak drive flux depends linearly to a very good approximation. This does not take account of the change in spectral shape that would actually occur and further reduce the ablation efficiency, but this is a small effect over the range considered, which is equivalent to radiation drive temperatures from ~250–315 eV. This range corresponds to laser energies between ~700 kJ and 1.5 MJ and was selected because it is approximately the range we envision using in NIF experiments to establish THD performance scaling experimentally during the initial NIC.

Figure 9(b) shows the burn averaged ion temperature, T_{ion}, plotted versus drive multiplier, x. A good fit to the simulated data is $T_{ion} = 1.87x + 1.05\text{keV}$, suggesting T_{ion} is

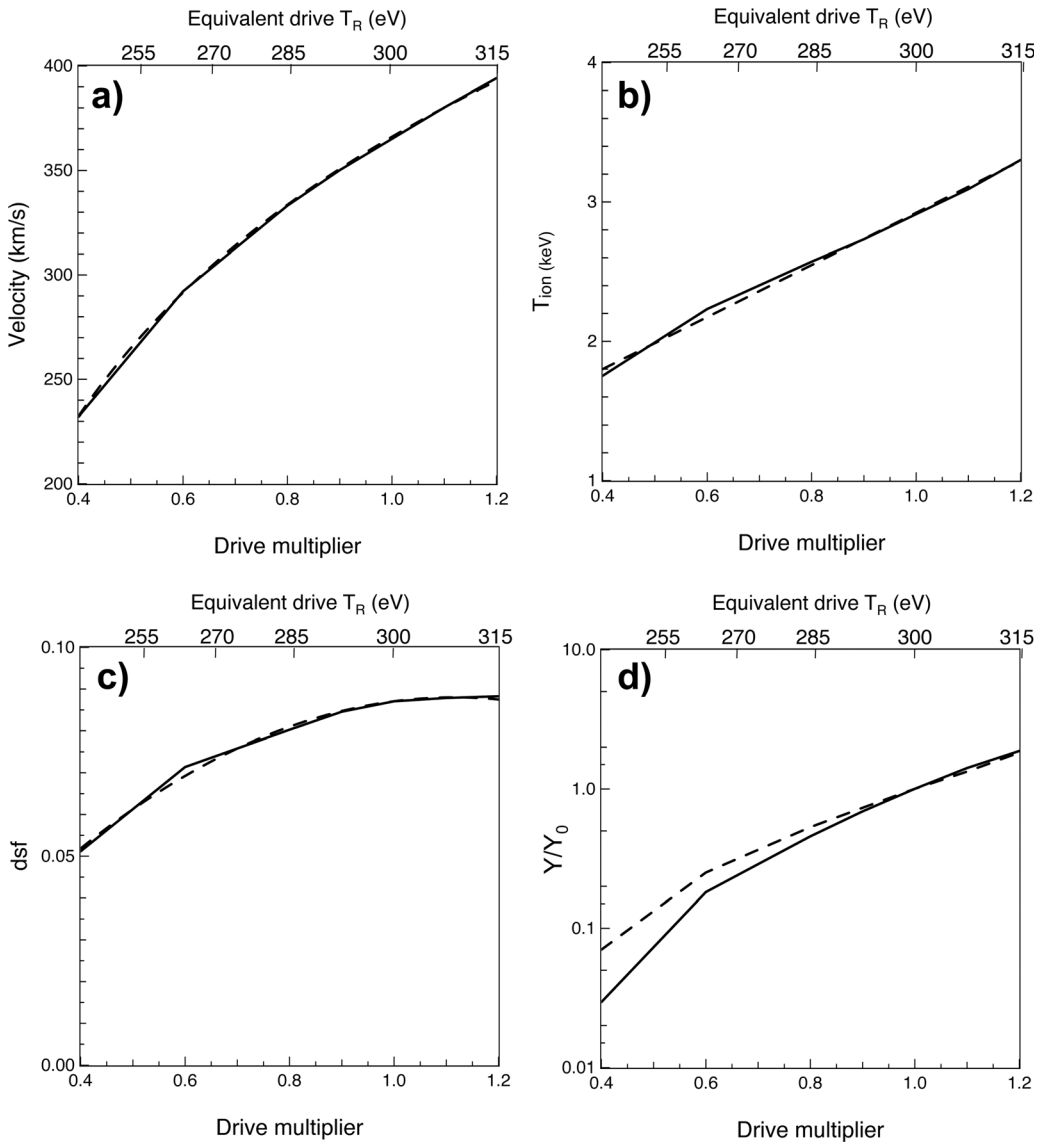

FIG. 9. (a) Simulated maximum implosion velocity of the fuel as a function of peak x-ray drive flux for the THD capsule shown in Fig. 2 (solid). The nominal x-ray drive ($x = 1$ corresponding to $T_R = 300$ eV) used is shown in Fig. 3. The drive amplitude was varied by multiplying the flux during the 4th (main) pulse by "x." The equivalent peak radiation temperature is also shown. The dashed curve is a logarithmic fit $V_{imp} = 146ln(x) + 366\text{km/s}$. (b) Simulated burn averaged hot spot ion temperature as a function of peak x-ray drive flux for the THD capsule shown in Fig. 2. T_{ion} is expected to vary linearly with velocity and therefore is also approximately linear in the drive [see Fig. 9(a)]. The dashed curve is the linear fit $T_{ion} = 1.87x + 1.05\text{keV}$. (c) Simulated burn averaged down scattered neutron fraction (dsf) as a function of peak x-ray drive flux for the THD capsule shown in Fig. 2. The dashed curve is the quadratic fit $dsf(\%) = -7.1x^2 + 15.8x$. (d) Simulated neutron yield as a function of peak x-ray drive flux for the THD capsule shown in Fig. 2. Over-plotted (dash) is the 1D scaling relation from Ref. 10, which reproduces the calculated behavior very well over most of the range.

exponential in implosion velocity. A fit which reproduces the data to better than 3% is $T_{ion} = 0.72exp(0.0038V_{km/s})$keV. Over the range considered here (~230–395 km/s and 1.75–3.3 keV), the scaling is reasonably approximated (better than 4%) by the nearly linear power law $T_{ion} = 0.0029V_{km/s}^{1.17}$ to be compared to the $V^{1.25}$ scaling derived in Ref. 9.

Interestingly, the total ρR is essentially velocity independent close to the nominal drive conditions as evident in Fig. 9(c) which plots dsf vs. drive. The near constancy of ρR occurs because most of the mass is in a shell, which is relatively thin compared to its radius. In a thin shell, the shell $\rho\Delta R$ is independent of the shell density and most of the total ρR comes from this thin shell of dense material. As the velocity falls farther from nominal, dsf, and therefore ρR, decreases gradually. The relationship between dsf and drive is well approximated by $\mathrm{dsf}(\%) = -7.1x^2 + 15.8x$ over the range shown. Finally the yield is plotted as a function of drive in Fig. 9(d). Also plotted is the 1D yield scaling from Ref. 10, $Y_{1D} \sim T_{ion}^{4.7}\mathrm{dsf}^{0.6}$ normalized to the nominal yield Y_0 at $x = 1$. Here we have substituted dsf for ρR. The scaling from Ref. 10 captures the variation extremely well over most of the range differing from the 2D simulations by just a few percentage for $<0.9< \times <1.2$. Below this, the scaling gradually departs from the simulations undershooting by about a factor of 2 when $x = 0.4$. This does not appear to be a 3D effect as the hot spot growth does not appear to be a strong function of the drive over the range considered. It is possible that as the drive falls substantially below the design conditions, the fraction of the shell that can effectively participate in compressing the fuel decreases.

At the upper end of the drive (velocity) range, the performance gain predicted in these simulations is likely optimistic. This is discussed in detail in Ref. 6 briefly, this is because high mode (ℓ~1000) mixing at the ice-ablator interface is not included in these simulations. In practice, as the drive is increased, the amount of mass shielding the inner ablator is reduced and preheating raises the Atwood number causing mixing between the ablator and fuel to increase, and eventually to penetrate the hot spot at which point it would rapidly quench burn. Precisely when this occurs as the drive (velocity) is increased is uncertain because the mix "front" is not a sharp front, but rather the CH has a distribution of penetration depths about the mix "front." Based on the structure of mix regions seen in highly resolved 2D and 3D simulations that resolve modes up to ~1000, it is estimated that ablator material will begin to penetrate the hot spot once the mix front has penetrated ~40% into the fuel (to be compared to 25% mix depth for the nominal point design,[6]). Here we have defined the mix front to be the location at which the mass fraction of CH averaged in the azimuthal direction is 5%; thus penetration is expected to occur first due to a few outliers of CH mix. We predict that enough additional ablator mass has been burned off once the drive has increased by ~20% above nominal (x = 1.2) for the mix depth to be approaching ~40% and hot spot penetration to begin. However, the precise way in which the gains in performance due to increased drive and velocity are offset and eventually overwhelmed by mixing of ablator material into the hot spot is uncertain and will need to be determined in experiments.

C. Sensitivity to shock timing and fuel entropy

The fuel adiabat or entropy will be optimized by a series of shock timing experiments which adjust both the strength and timing of the shock waves launched into the capsule by the shaped pulse of the form shown in Fig. 3. A detailed description of these experiments and sequence can be found in Ref. 7. To illustrate the effect of shock timing experiments on implosion performance, consider the following. The largest uncertainty in setting the laser pulse prior to experiments is in the laser power needed in the first pulse to obtain the desired x-ray drive and shock velocity. This is because during the first pulse the laser beams initially propagate through cold material and conditions change rapidly making the x-ray drive sensitive to laser pulse variations. Once the first pulse laser power has been set, all the other shocks must be timed relative to this. After the shock timing experiments have been completed the largest remaining error is expected to be in the launch time of the fourth pulse.[7] For these reasons above we have performed an ensemble of 1D and 2D simulations starting with a near ideal shock timing and varied the first pulse level about nominal by up to ±60%, causing all the other shocks to become significantly mis-timed. We have also varied the launch time for the fourth pulse independently. The simulations used a peak drive consistent with a 1 MJ laser pulse. Figures 10(a)–10(d) shows the predicted sensitivity of implosion parameters to these variations. The results are quite striking. As can be seen in Fig. 10 the dsf (or ρR), hot spot radius, ion temperature and yield all trend with the fuel entropy which is a direct measure of how well the shocks are timed. There is no significant distinction between trends seen in 1D and 2D results, which is to be expected since this is largely a 1D effect. The observed trends cannot be attributed to changes in implosion velocity, which for the most part are small for the shock timing changes made. One way to quantify this is to consider the mean and standard deviation of T_{ion} for the simulations shown in Fig. 10, 2.5 ± 0.4 keV, while the velocity distribution is 304 ± 12km/s. The variation in temperature due to this ±12km/s velocity variation (with nothing else changing) can be estimated for the data in Fig. 9 as just ±0.1 keV compared to the simulated width of ~0.4 keV.

The strong correlation between the implosion dsf (or ρR) and fuel entropy is expected.[10] Using the following fit to in-flight adiabat in terms of fuel entropy $\alpha_{if} \approx [1 + \exp\{(s - 0.455)/0.063\}]^{0.54}$, we find the dsf data scales as $\alpha_{if}^{-0.7}$ compared to $\alpha_{if}^{-0.54}$ in Ref. 10. Similar agreements are found for T_{ion} proportional to $\alpha_{if}^{-0.2}$ vs $\alpha_{if}^{-0.15}$ and hot spot radius proportional to $\alpha_{if}^{-0.36}$ vs $\alpha_{if}^{-0.2}$ from this work and Ref. 10, respectively.

D. Sensitivity to surface roughness

To evaluate the effect of surface roughness on implosion performance, we have varied the outer ablator surface and inner ice surface independently for targets driven at ~1 MJ and ~1.3 MJ. The set up used was that described in Secs. II A and B. The surfaces were varied by applying a uniform multiplier on the modal amplitudes, against which implosion performance is plotted in Fig. 11(a) for ablator roughness

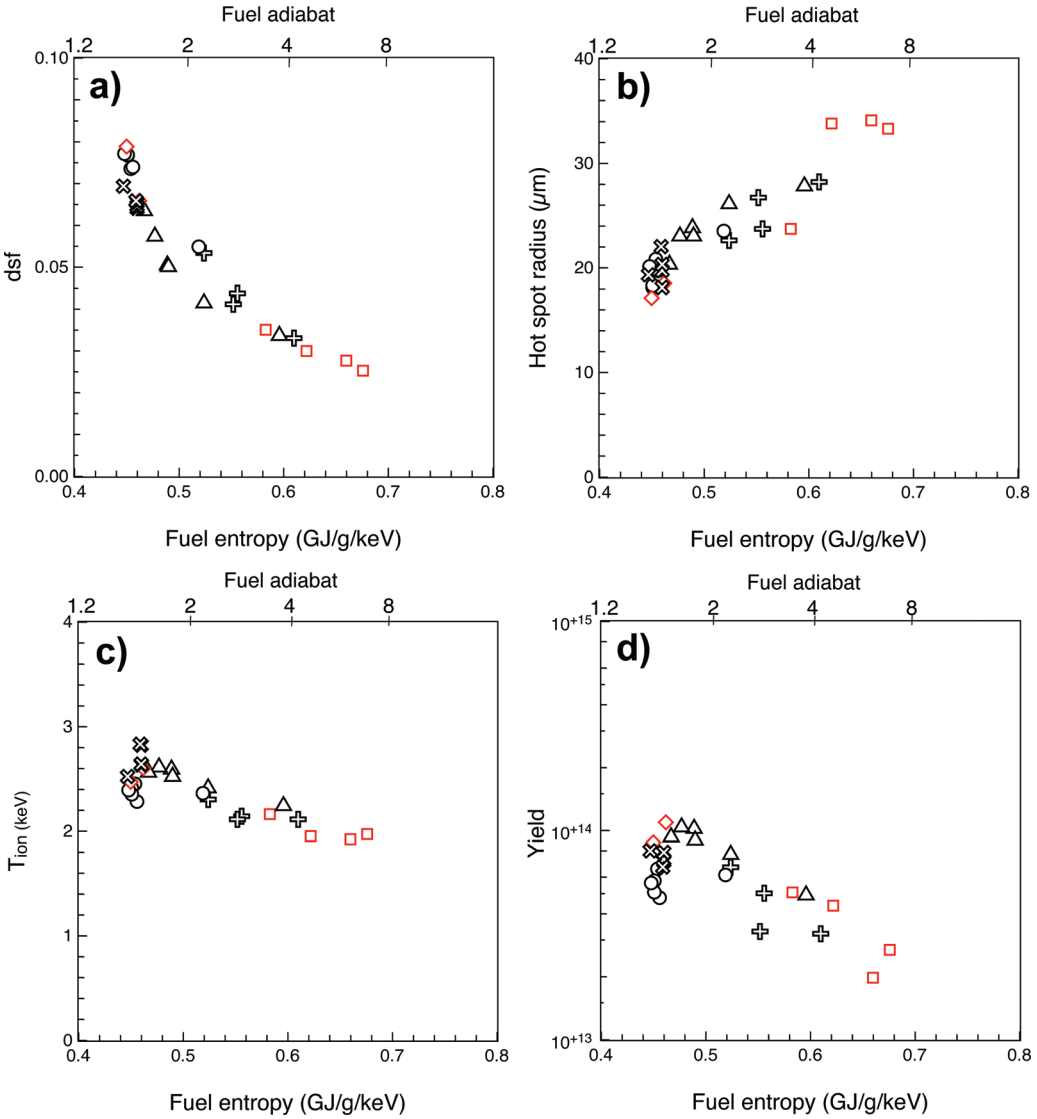

FIG. 10. (a) (Color) Simulated down scattered neutron fraction vs. mass averaged fuel entropy (adiabat) at peak velocity from ensemble of 1D and 2D simulations for the capsule show in Fig. 2 in which various shock mis-timings have been introduced. The peak drive was ~285 eV equivalent to a laser energy ~1 MJ. The composition was as described in Sec. III (for the solid layer—H:D:T = 24:2:74; for the central gas at $t = 0$ H:D:T = 0.92:0.0078:0.072). 1D results are red, but show the same quantitative trend as the 2D results. Key: squares, up to ±60% 1st shock level combined with −200 ps 4th shock mis-timing; crosses, ±35% 1st shock level mis-timing only; triangles, 4th shock advance between −100 and −400 ps (dsf reduction increases as shock advance increases); 45° crosses, nominal shock timing with up to ±40% asymmetry in the imploded configuration (has little effect); circles, 4th shock delay by up to 400ps; diamonds, nominal 1D simulations. (b) Simulated x-ray image sizes for the set of simulations described in Fig 10(a). The size increases monotonically as the fuel entropy/adiabat or degree of shock mis-timing increases and compressibility decreases. (c) Simulated burn averaged ion temperatures for the set of simulations described in Fig 10(a). A similar trend to the other observables is seen. (d) Simulated neutron yield for the set of simulations described in Fig 10(a). The theme of performance vs shock timing holds for yield also. However the spread in the values due to other effects such as 1D vs 2D and small velocity changes as the shocks are delayed, for example, are more obvious in this observable.

and Fig. 11(b) for ice roughness. We discuss ablator roughness first.

The variation in yield as the ablator outer surface roughness and therefore in-flight ablator modulation is varied is shown in Fig. 11(a). For 1.3 MJ the yield begins to roll off, once the roughness increases beyond ~2 × nominal. Several effects contribute to this. Ablation front perturbations begin to feed through to the hot spot, but more significantly, the ablation front growth distributes the main fuel layer over a larger radial extent making it a less efficient piston reducing the hot spot temperature and yield. Accompanying this is a steady reduction in dsf (ρR) by ~30% as the surface roughness is increased from nominal to 6 × nominal. While there is some increase in fuel entropy as the roughness increases, the dominant effect is the lower effective ram pressure in the main fuel layer. The situation for a 1 MJ drive using the same capsule is similar but the roll off in performance is offset by ~ × 2 compared to the 1.3 MJ case. The simple interpretation of this is that ablation front growth factors in our simulations are predicted to be ~2 × more at 1.3 MJ than at 1 MJ.

Figure 11(b) shows the yield decreasing monotonically as a function of ice surface roughness for both 1 MJ and 1.3 MJ cases. This is almost entirely due to reduction in hot spot clean volume as the roughness is increased; neither T_{ion} nor dsf change appreciably.

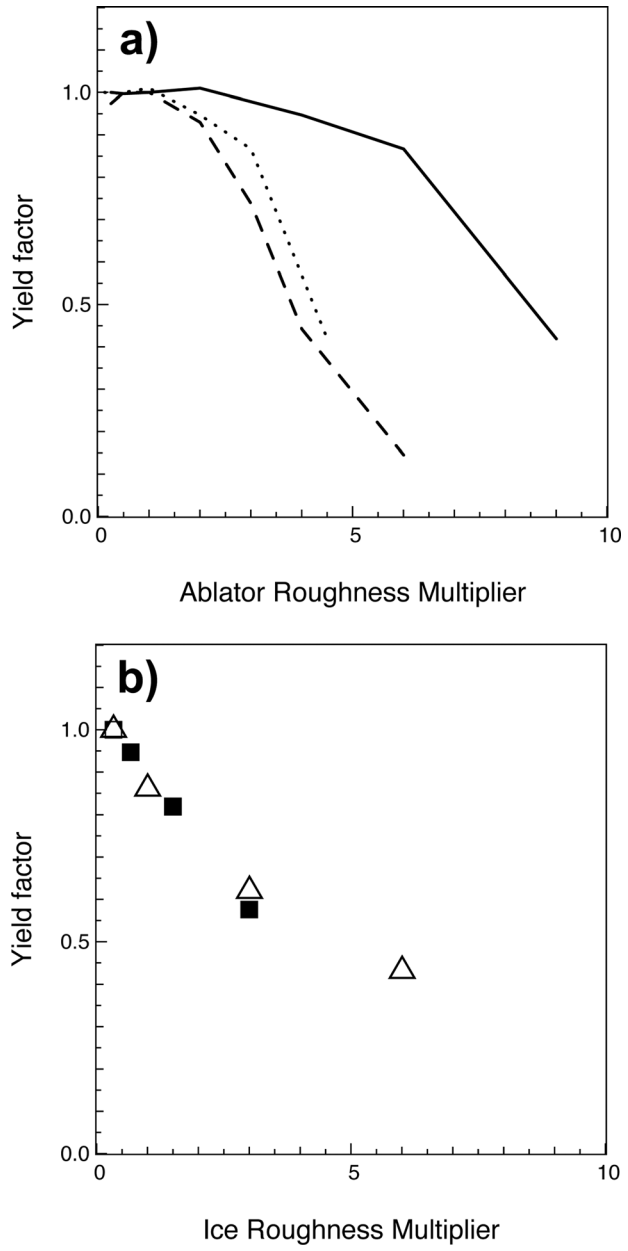

FIG. 11. (a) Simulated neutron yield as a function of ablator roughness for 1 MJ (solid) and 1.3 MJ (dash) implosions of the capsule shown in Fig. 2. The surface was varied by applying a multiplier (*x*-axis) on the surface form shown in Fig. 8(a). Also shown (dot) is the 1 MJ curve plotted as if the roughness were only 50% of that applied. This curve is close to the 1.3 MJ curve because the predicted ablation front growth factors at 1 MJ are ~50% of those at 1.3 MJ. (b) As Fig. 11(a) but for inner ice surface roughness. In this case there is no difference between the scaling between 1 MJ (triangles) and 1.3 MJ (squares). We attribute this to two factors. First the ice roughness is the dominant effect reducing hot spot yield in these simulations. Second both 1 and 1.3 MJ implosions undergo similar deceleration growth so that the yield degradation is similar in both cases.

V. DIAGNOSTIC SIGNATURES OF IMPLOSION PERFORMANCE

The key performance parameters v, α, s, m and variables ρR, T described above must be inferred from experimental measurements. A detailed description of techniques used to infer v, α, s, m during the tuning campaign can be found in Ref. 7. In this section the key signatures from targets with THD and DT fuel layers are discussed. These implosions emit copious amounts of photons and neutrons, which encode in their spectra much of the target performance information we need to know. When complemented and augmented by spatial imaging, reasonably complete diagnoses of the implosions can be made. In the case of THD implosions only the central hot spot containing ~5–10% of the total fuel mass becomes hot enough to radiate x-rays and nuclear products. The surrounding dense fuel is too cold to emit but can be diagnosed by using the hot spot radiation, particularly neutrons, as a self-probing source. Active probing by a separate source, which for practical purposes would be x-rays, is also possible. In the case of burning DT targets, the entire fuel becomes hot so that the emission source extends over the whole fuel. Because burning plasmas are extremely bright, the emitted radiation is currently the only practical means of diagnosis. The diagnostics signatures from THD followed by those from DT implosions are discussed in the following section. It is convenient to separate the discussion in to x-ray and neutron signatures.

A. THD x-ray diagnostic signatures

The x-ray spectrum emitted from a typical THD implosion is shown in Fig. 12. The majority of the x-ray emission when no ablator material is present in the hot spot is bremsstrahlung, for which the emissivity is

$$P_{h\nu} \propto g\frac{n^2}{T^{1/2}}exp\left(-\frac{h\nu}{kT}\right),$$

where P is the emitted power at photon energy hν from a hot spot with density n and temperature T, and g is the Gaunt factor for free-free transitions. Notably, the bremsstrahlung spectrum falls exponentially with increasing photon energy

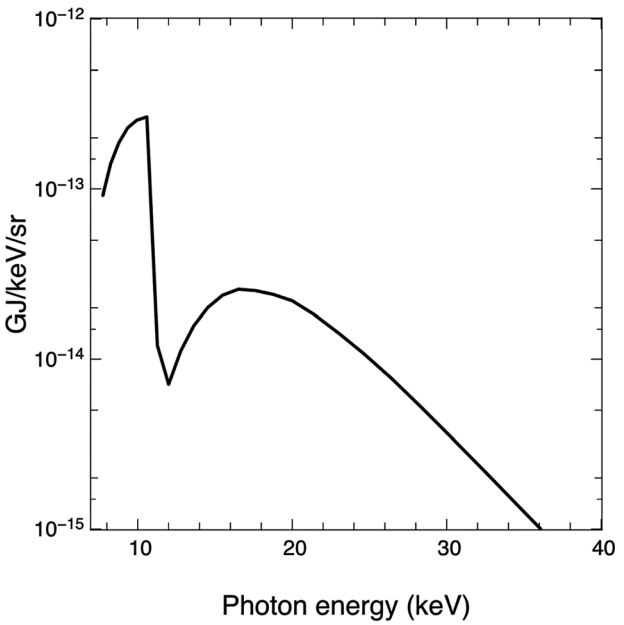

FIG. 12. Predicted x-ray spectrum at peak x-ray power for a nominal THD implosion meeting design requirements. The spectral emission peaks at ~10 keV. The cut off on the low energy side is due to attenuation by the dense fuel shell. The fall off on the high energy side follows the bremsstrahlung relation. The dense shell is effectively optically thin above ~30 keV. The K-edge due to Ge in the ablator can be seen clearly at about 10 keV.

with a slope given by the plasma temperature. If the temperature can be established, the absolute emission gives information on the plasma density, which can be used to infer ρR_{HS}. In practice, this analysis may be complicated because small amounts of ablator material can be mixed into the hot spot, and the material surrounding the hot spot absorbs some of the radiation.[22] The opacity due to bremsstrahlung uncorrected for stimulated emission is

$$\kappa_{h\nu} = 2.78 \frac{Z^3 \rho}{A^2 T^{1/2} (h\nu)^3} \mathrm{cm}^2/g,$$

which decreases as the cube of the photon energy. Here ρ is in g/cc, and T and hν are in keV. The result is that the bremsstrahlung emission observed in THD experiments is expected to be peaked around ~10 keV. At high photon energy $\geq$ 20 keV the radiation effectively escapes unattenuated, making this portion of the spectrum a potential diagnostic of the plasma temperature.

Below ~20 keV the hot spot emission becomes progressively more attenuated by the surrounding dense shell, consisting of cold fuel ($\rho R \sim 1.4$ g/cm^2) and some remaining ablator material ($\rho R \sim 0.3$ g/cm^2). Little radiation escapes below ~5 keV. In principle emission between 5 and 10 keV could be used to probe the surrounding shell when the emission is imaged. However, it can be difficult to distinguish hot regions in the core from thin spots in the shell, and the remaining ablator material further complicates the picture. This degeneracy may be alleviated by adding energy discrimination in the images and more diagnostic lines of sight. In NIF experiments, it is planned to have at least two lines of sight, one on the hohlraum equator and one along the pole (axis of the hohlraum).

A sequence of simulated gated x-ray images is shown in Fig. 4(c) for filtering selecting x-rays with energies above 10keV. The gate time is 70 ps, which is typical of the detectors used on NIF and other facilities.[28] The energy band has been selected to best represent the size and shape of the hot spot. Lower energy x-ray images tend to capture more of the hot spot, whereas higher photon energies preferentially weight the hottest central region, gradually becoming rounder as the energy is increased. The size of the images compared to the actual hot spot size is shown in Fig. 13. As can be seen the x-ray image quantitatively approximates the hot spot size and tracks it in time. The size of the image is referenced to the contour that is ~20% of peak brightness as this has been found to best represent the hot spot size and is typically located with high accuracy with the number of photons expected to be emitted.

In general it is found through numerous radiation hydrocode simulations that the P_2 distortion of the gated x-ray image taken at peak brightness is a very good measure of the actual P_2 hot spot distortion (<5% difference) for a THD target and for the equivalent DT target at ignition time. For P_4, there is typically a small offset ~10% provided the P_2 distortion is <25%, beyond which the P_4 from the image can depart rapidly from that of the hot spot. In practice, 3D effects from such things as power balance and pointing errors, as well as capsule shape variations, introduce additional errors in the interpretation of, for example, P_2. These have been estimated from 3D hydra simulations to be ~3% for the magnitude of 3D effects anticipated. In the case of the 3D simulations, the x-ray image contour was compared with a density contour taken around the hot spot in the mid plane of the implosion perpendicular to the line of sight.

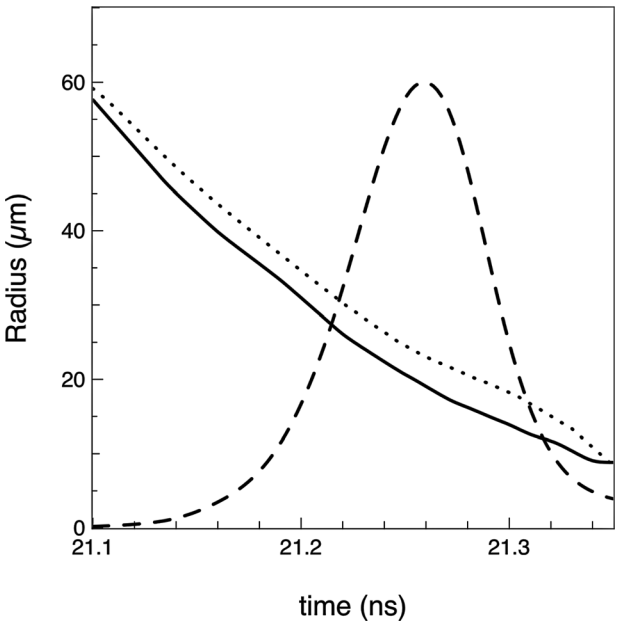

FIG. 13. P_0 coefficient of the 20% contour vs time from gated x-ray images filtered for >10 keV for a THD implosion simulation (solid). The radius of the hot spot (50% density surface) is also shown (dot). As can be seen the x-ray images are slightly smaller than the hot spot, but the size is otherwise well approximated. The normalized emitted power is plotted for reference (dash).

The x-ray emission can also be imaged using a time integrating diagnostic, which emphasizes the time of peak emission. This is typically the time of most interest, but informative dynamic information is lost.

B. THD neutron diagnostics signatures

The main nuclear reactions producing neutrons are the DT, DD and TT reactions,[5]

$$\begin{aligned}
&D + T \rightarrow {}^4\mathrm{He}\ (3.5\mathrm{MeV}) + n(14.1\ \mathrm{MeV})\\
&D + D \rightarrow T(1\mathrm{MeV}) + p\ (3\ \mathrm{MeV})\\
&D + D \rightarrow {}^3\mathrm{He}\ (0.82\ \mathrm{MeV}) + n(2.45\ \mathrm{MeV})\\
&T + T \rightarrow {}^4\mathrm{He} + 2n + 11.3\ \mathrm{MeV}.
\end{aligned}$$

The DD reaction produces a neutron along one branch and a proton along the other with roughly equal probability. The TT reaction produces two neutrons over a broad spectrum up to ~9.5 MeV and swamps the signature from the DD reaction in THD implosions which have only a small amount of D. The TT reaction is less well understood than the DT (or DD) reaction, which is of most interest for diagnostic purposes since it has a well established cross-section and produces a neutron with a well defined energy (14.1 MeV) (Fig. 14).

A significant fraction of the 14 MeV DT neutrons (primaries), ~75%, leave the target without undergoing a collision. They can be imaged without temporal gating and are similar in character to time integrated x-ray images captured

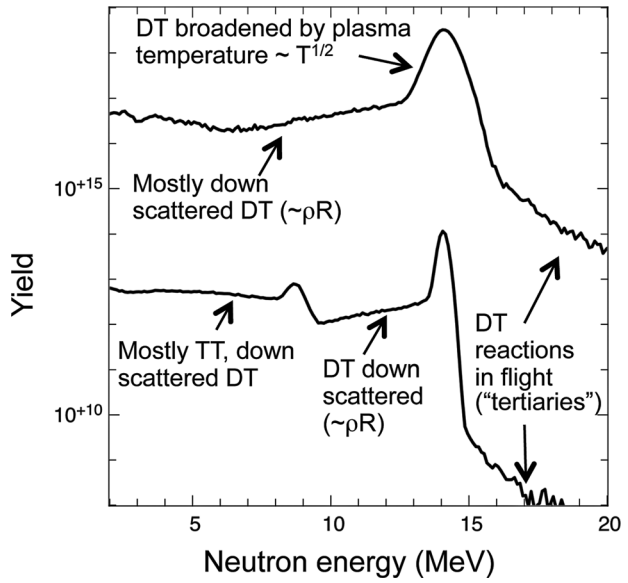

FIG. 14. Simulated neutron spectrum from THD (2%) (lower curve) and equivalent igniting DT target (upper curve) showing how important physics signatures are related to various parts of the spectrum.

at ~25 keV photon energies. The energies of the 14 MeV neutrons are broadened by the thermal motion of the plasma with a width in keV of $\sim 177\sqrt{T_{keV}}$, providing information on the plasma temperature.[11] The remaining ~25% of the neutrons scatter off a target nucleus before leaving the plasma. The vast majority of these collide with the thermal background of ions in the dense fuel and emerge at lower energy as part of the "down scattered" signal,

$$n(14.1\text{MeV}) + H \Rightarrow n' + H(0 - 14.1\text{MeV})$$
$$n(14.1\text{MeV}) + D \Rightarrow n' + D(0 - 12.5\text{MeV})$$
$$n(14.1\text{MeV}) + T \Rightarrow n' + T(0 - 10.5\text{MeV}).$$

The magnitude of this signal is proportional to the target ρR and is the main source of neutrons from ~9.5 to 12.5 MeV, containing ~20–25% of the scattered neutrons.

Finally, a small fraction of the neutrons (tertiaries) is born above 14 MeV, producing a high energy tail to the spectrum. These arise from DT reactions between a thermal D(T) and a T(D) that has been up scattered in a previous collision with a 14 MeV DT neutron or a 3.5 MeV α-particle. This is a third order effect and likely too weak at THD yields to be useful, although it should provide ρR information in DT experiments with high yield.

C. THD down scattered neutrons and shell ρR

The dsf is approximately proportional to fuel ρR, with most of the down scattering occurring in the dense shell surrounding the hot spot. For THD implosions there is an energy window between ~10 and 12 MeV sitting between the TT neutrons and the Doppler broadened DT primaries that is populated by neutrons down scattered from 14 MeV. This is typically the window that is used to define the dsf for THD implosions.

A measurement of the dsf (# neuts in 10–12 MeV)/(# neuts in 13–15MeV) is an intuitively and conceptually appealing idea for measuring $<\rho R>$, and requires only a neutron fluence measurement with reasonable energy discrimination. However, there are some important subtleties that must be taken into account. Consider Fig. 15, which shows the results from a 3D hydra simulation with relatively large shell ρR variations (~2:1). The laser beams in this calculation were configured to produce a large $Y_{4,4}$ asymmetry. Such an asymmetry could be possible in early experiments if the locations and relative brightness of the inner beam spots on the hohlraum wall were found to be different from initial predictions. No other sources of asymmetry such as laser power balance or capsule non-uniformities were included, but these are expected to result in much smaller variations than imposed here. Despite the large shell ρR non-uniformity, this would not be evident from self-emission images of the hot spot (x-ray or neutron), which remained relatively round with an RMS deviation of only 12%.

The first graphic in the figure is an equal area projection map of $<\rho R>$ vs (θ,ϕ) of what is effectively a quasi-spherical shell of dense matter in the imploded configuration. Because the neutron scattering angle is related to the energy of the scattered neutrons and depends on the mass of the scatterer, the 10–12 MeV neutrons observed from a given line of sight effectively sample only a fraction of the total

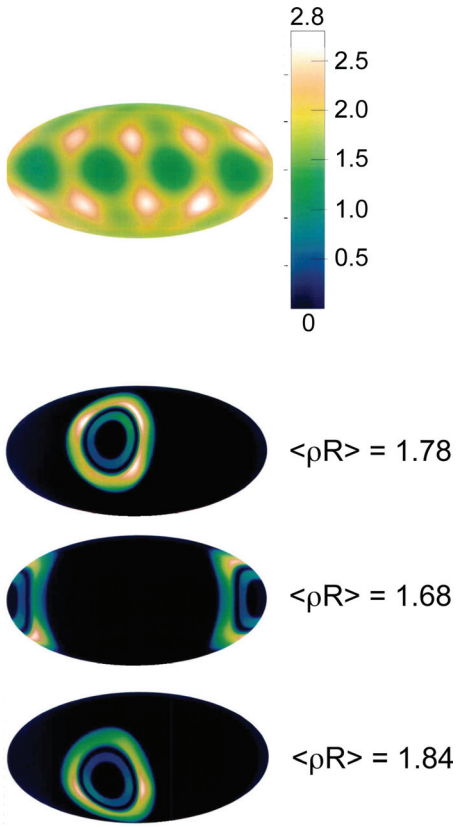

FIG. 15. (Color) World map of THD fuel ρ-R at stagnation from a 3D hydra simulation deliberately engineered to have a large $Y_{4,4}$ asymmetry resulting in ρR variations ~2:1. The section of the shell probed by neutrons (assuming a central point source) scattered into the 10–12 MeV energy range are shown for three of the neutron spectrum detectors on NIF. The central dark region is the section of each LOS sampling the primary 13–15 MeV neutrons. The ρR inferred along each line of sight from the dsf varies because both "primary" and scattered neutrons vary because of the shell ρR variations.

solid angle of the shell. The bulls-eye patterns in the accompanying graphics represent scattering by tritium (the outer, brighter ring) and by hydrogen (the inner, fainter ring). The hydrogen ring is fainter and narrower than the tritium ring because there is only $1/3$ as much hydrogen and its cross section is smaller. The ring width is kinematic. The effective views are shown from three lines of sight corresponding to the given (θ,ϕ)'s and the three $<\rho R>$'s obtained by averaging over the rings viewed. The tritium and hydrogen rings represent a sample of about $1/10$ of the sphere. Taking into account the small (for THD) but finite size of the 14 MeV source (i.e., hot spot), the fraction is about $\sim 1/9$ of the total solid angle—leading to the possibility of a bias or "sampling error" due to spatial variations in the shell. The ρR sampled in this way can vary by up to $\pm 10\%$ along any of the lines of sight depending on the azimuthal orientation of the capsule with the diagnostic views. Because each of these is close to the equator they see similar variations. The average of all three views, however, never deviates by more than $\pm 4\%$ from the solid angle averaged value. This increases to $\sim \pm 8\%$ for a two view average. This represents the sampling error in the numerator of dsf. The denominator also varies considerably from LOS to LOS. Scattering and other processes, such as $(n, 2n)$, *remove* neutrons from the 13 to 15 MeV range. The "optical depth" for this effect is proportional to the LOS ρR: $\tau = 0.165$ $(\mathrm{cm}^2/\mathrm{g})^*$ ρR for THD. For the 2:1 variation in ρR, shown in Fig. 15, leads to a 24% variation in the denominator of dsf. The dsf then represents a mix of 3 geometrically different samples of ρR: The two bulls-eye rings shown in Fig. 15 and a small spot in the center of the rings for the 13–15 MeV neutrons, representing about 4% of the area.

These sampling effects have also been evaluated using a large ensemble of 2D simulations of the type described in Sec. IV which include higher modes due to surface roughness as well as drive asymmetry. *A priori*, we expect most 2D variations in ρR to be approximately axisymmetric about the hohlraum polar axis. Given the ring pattern of scattered neutrons, a polar LOS would be expected to be a poor choice to represent a mean dsf value and that views from varying ϕ's and from varying θ's near but not all on the equator would do better at averaging over ρR fluctuations. With a sample of about 700 different 2D simulations in which entropy, shape, velocity, and mix were uniformly varied by $\pm 1\sigma$ about the point design values, we found that the numerical average of three dsf 's as determined from the three LOS's shown in Fig 15, differed by $\leq 2\%$ rms from dsf that would have been found with an omni-directional neutron detector. Because there is an intrinsic scatter of $\sim 15\%$ in dsf for a given ρR, cf. Fig. 16, these three LOS's for neutron detectors approach the point of diminishing returns, whereas 3D simulations showed that averaging over two LOS's provides significantly less accuracy than the three lines of sight that have been selected for initial NIF experiments to sample dsf.

The relationship between dsf and ρR is shown in Fig. 16, which shows burn averaged fuel ρR (weighted by the burn rate averaged spatially, and over the burn width) plotted against the total (integrated over all directions) down scattered fraction (10–12 MeV) for the large 2D simulation data base described above. The mapping is not precisely one to one in part because of degeneracy in the geometrical definition of ρR, i.e., different spatial configurations which will have different down scattered fractions can have the same ρR. In addition to this, there is a more subtle dependency worth noting. Mixing between the ablator and fuel displaces some of the fuel to larger radius, reducing fuel ρR and replacing it with ablator material which has a lower cross section for scattering. Based on the numerical data base these effects could reasonably produce a 1σ uncertainty in ρR of $\sim 7\%$ for a measured down scattered fraction.

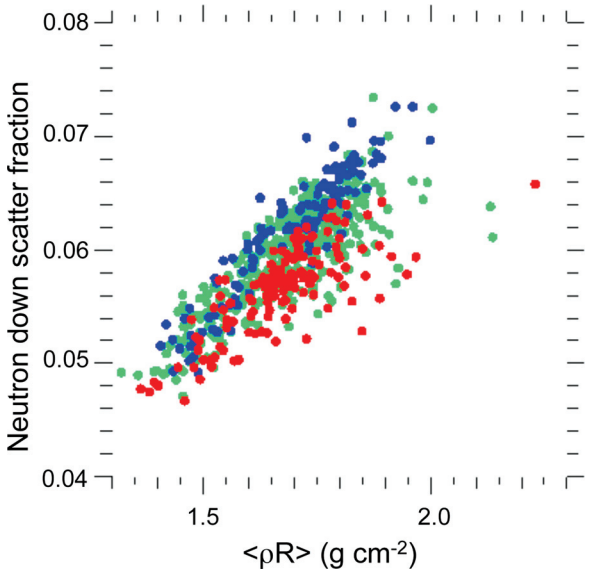

FIG. 16. (Color) Correlation between ρR vs down scatter fraction averaged over 4π from a large 2D simulation data base (green). The down scatter fraction is sensitive to the amount of mixing between the ice and ablator [(red) highest 20% vs (blue) lowest 20%]. In the absence of additional information about mixing this introduces an uncertainty in $\rho R \sim \pm 7\%$.

D. DT diagnostics signatures

The important diagnostics signatures from igniting DT targets are much the same as those from THD's with some important differences. The temperature of the plasma is about an order of magnitude larger and the thermonuclear burn wave propagates through the entire fuel, which becomes hot and radiates. Thus neutron (and x-ray) images of the core are much larger than in THD implosions (Fig. 17). The neutron spectrum is dominated by neutrons originating from DT reactions. The DT peak ($\sim$14 MeV) in the neutron spectrum is significantly broadened by the higher temperature (Fig. 14). The much higher pressures in igniting DT targets cause the fuel to disassemble in $\sim$10 ps; once ignition has occurred, compared to $\sim$100 ps for a THD, which is reflected in a much shorter γ-flash from nuclear reactions in the fuel as described below.

E. Diagnostics

A large number of diagnostics will be fielded to measure the performance of THD and DT implosions. As described above, the key performance metrics are the size and shape of

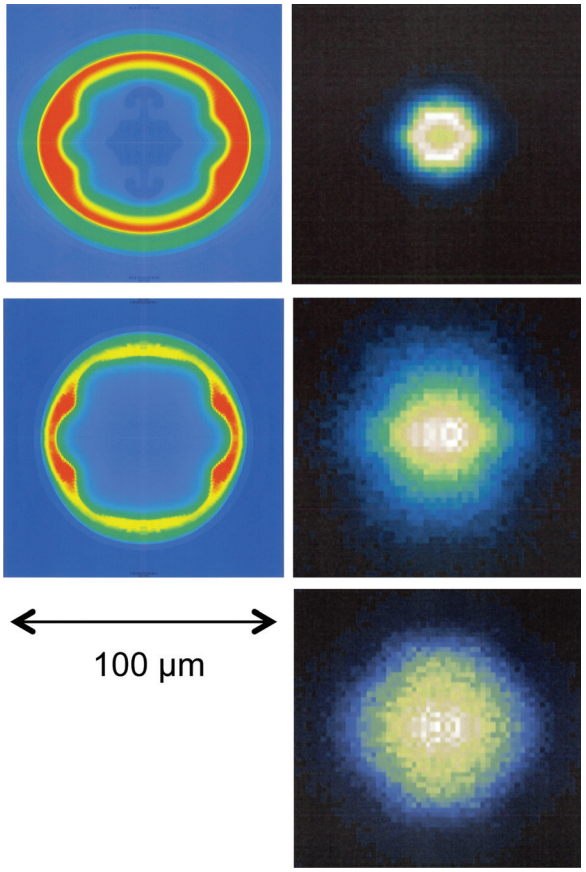

FIG. 17. (Color) Density maps at peak energy production and time integrated primary neutron images (13–20MeV) for THD (top), 1.6 MJ yield DT (middle), and 12 MJ yield DT (bottom) implosions. These are integrated hohlraum simulations that resolve up to mode l~8 from drive asymmetry alone. No other sources of perturbation have been included. No density image is shown for the DT target because the explosion is very rapid. The THD is the equivalent of the 1.6 MJ DT implosion. The neutron image is weighted towards the central, hottest portion of the hotspot, which grows as the burn wave propagates further with increasing yield.

the hot spot, the x-ray spectrum, the neutron yield and fraction of neutrons scattered from the fuel (ρR), and the burn history. The principal diagnostics are summarized briefly below.

A key feature of the THD implosions is that the neutron yield can be controlled via the %D concentration in the fuel to optimize the diagnostics environment. It is expected that x-ray imaging will be feasible on NIF, without special relay optics to a shielded location, for neutron yields up to $\sim 10^{15}$ using a hardened gated x-ray imager (hGXI).[29] This provides a large number of snapshots of the implosion for hot spot size and shape. Each image integrates over ~35–70 ps and a total interval ~800 ps can be covered, compared to the ~100 ps of the THD emission time. The spatial resolution of the hGXI is ~5–10 μm compared to the ~25 μm diameter of the x-ray image at a peak brightness. Different filtering can be used to provide spectral discrimination on the same shot in order to extract temperature information.[30] A similar diagnostic, being built to operate in the 10^{17} range for implosions with higher %D fills, must be located outside the target chamber with adequate shielding against the higher neutron environment. A faster camera is under development to provide ~10 ps resolution, which is on the same order as the burn width of igniting targets.

A neutron imager will also provide time integrated spatial information of the hot spot.[31] The detector will be a stacked fiber scintillator located 28 m from the target, imaged by two cameras to produce one image of the primary neutrons, between ~13 and 20 MeV, and another gated from 10 to 12 MeV showing neutrons scattered within the capsule.[32] Figure 17 shows a calculated primary image of a THD capsule. Because the central gas in a THD capsule has a very low deuterium and tritium content, in the absence of mix between the fuel gas and the ice, little DT yield is produced in the center of the implosion; all the yield comes from material that was originally ice. The primary image shows a dip in the center, which is removed as ice mixes into the gas during the implosion. Thus the radial profile of an image, if it could be resolved, would be sensitive to gas/ice mixing. X-ray production is not sensitive to the isotope composition and is centrally peaked as are x-ray images. For a DT capsule the central gas is as reactive as the ice and this effect is eliminated. As the deuterium content of a THD capsule increases and fusion particle energy deposition affects the hydrodynamics, the neutron images increase in size. The calculated primary image for the ignited DT version of the same capsule is also shown in Fig 17.

The neutron spectrum will be measured by several diagnostics. A number of neutron time of flight detectors[33] will be used to measure the primary DT neutron yield and azimuthal variations, burn averaged ion temperature, and the fraction of neutrons scattered by the fuel, which is proportional to ρR. A number of detectors are required to cover the large range in neutron yields for THD and DT implosions. Several detectors are located at ~4 m from TCC and measure prompt signals (Y, BT) for the lower yield THD targets. An additional four detectors (two independent lines of sight) will be located at ~20 m from TCC. These allow the neutron signal to dilate in time making it easier to measure the spectrum for ion temperature and the down scattered fraction. For DT yields the close in detectors will no longer work and the 20 m detectors are relied on for all spectral information.

The neutron spectrum will also be measured quantitatively using a magnetic recoil spectrometer which provides an additional line of sight.[34] This converts the neutron signal to a proton signal via collisions in a CH target foil. The proton spectrum is then measured by dispersing them spatially on to CR39 using a magnet. This diagnostic has been designed to work for the entire range of neutron yields from THD and DT targets.

Neutron activation detectors containing Zirconium [Zr90(n,2n)Zr89] will measure yield at several different azimuths to complement the nToF and Magnetic Recoil Spectrometer detectors. The threshold energy for activation is ~12 MeV making this suitable for measuring the primary DT neutron signal. The yield is inferred by measuring absolutely the ~909 keV γ-ray yield from the activated Zr nuclei. This is similar to copper activation technique, but unlike Cu the Zr has a much longer half-life (~3 days vs 10 min),[35] making it functionally easier to implement. In principle a number of detectors can be fielded at different azimuthal locations to measure target ρR variations. A similar technique was fielded on recent NIF experiments to measure DD neutron yields using indium.

The capability to field capsules with radiochemical tracers is being implemented on NIF. There are several potential applications, one of which is to measure the ρR of the fuel. The tracer material in this instance is ^{124}Xe loaded into the inner region of the ablator. There are two nuclear reactions of interest, the ^{124}Xe $(n,2n)^{123}$Xe and ^{124}Xe$(n,\gamma)^{125}$Xe reactions. The former is sensitive to neutrons with energies $\leq$10 MeV, while the latter has a threshold $>$ 11 MeV. The ratio of the two product nuclei is similar in nature to the dsf obtained from the ratio to the number of scattered neutrons to primary neutrons. Numerical simulations have found a very strong correlation between the ^{123}Xe:^{125}Xe ratio and dsf.

The gamma ray reaction history (GRH) or "burn history" will be measured using a four-channel gas Cherenkov γ-ray detector[36] located 6 m from TCC. The γ's impact a converter foil producing electrons, which then produce Cerenkov radiation in the gas cells. The four cells will have different gas densities to produce gamma thresholds of 3, 5, 8, and 14 MeV. Data from these will be used to obtain the total yields and time history of three capsule gamma rays; 16.7 MeV gamma rays from a branch of the D + T reaction, 19.8 MeV from T + H reaction, and 4.4 MeV from neutrons interacting with the carbon in a plastic ablator. Neutrons passing through the Au/U/Al hohlraum wall produce a background of gamma rays delayed from the prompt signal, which must be subtracted. There is some evidence that burn history can be used to help discriminate yield degradation due to large asymmetries from small scale mixing.[37] The time dependent ratio of the 4.4 MeV to the 16.7 MeV gammas is proportional to the carbon (or plastic) ρR. Finally the combined information from the 16.7 MeV γ and the 19.8 MeV γ diagnose the H/D ratio in the burning fuel. This is of interest because it is indicative of the degree of mixing between the cold fuel and the central gas region. As discussed earlier the central gas region in the capsule is initially hydrogen rich and effectively dudded unless DT from the ice layer mixes into it. The temporal resolution of the GRH will initially be limited to ~100 ps by the optical diode used to resolve the Cherenkov signal, but will later be improved to ~20 ps by using a streak camera. Since the high energy channel selects γ-rays from the fusion reactions, this diagnostic should provide a good diagnostic of the fuel burn history.

Information about areal density and shape of the dense cold fuel surrounding the hot spot can be obtained by active probing using an external source of hard x-rays, i.e., by recording radiographs from x-ray backlighters. These images can in principle be obtained using transmission Compton radiography,[38,39] where high energy Compton scattering is used rather than traditional photo-absorption to cast a shadow of the imploding capsule. The Compton scattering cross section is largely independent of photon energy for photon energies of 50–200 keV. As a consequence, the optical depth of the fuel of an ICF target shows a plateau above ~50 keV, where the Compton scattering dominates.

Because of the slow dependence of the Compton scattering cross section on the x-ray photon energy, the areal density of the fuel can be inferred even using a polychromatic backlighter. A broadband bremsstrahlung emitting source should be adequate and the energies of the x-ray photons can be selected by a combination of a high-pass filter and the detector response to optimize signal to background.[39] In this application a major source of background will be the self-emission from the stagnating capsule, which is concentrated largely below ~20 keV, but should be readily filtered out. Using hard-x-ray photons will also minimize the refraction of the probing x-ray beam as it traverses the shell so that the spatial resolution remains close to the backlighter source size.

This Compton radiography technique has been demonstrated recently on direct drive implosions at the OMEGA laser facility,[40] where radiographs of imploding plastic shells have been recorded with ~10 μm and ~10 ps spatial and temporal resolution, respectively, at photon energies around 100 keV.

On the NIF, we plan to generate the radiographs using 10 μm-diameter Au wires in an end-on, point-projection geometry.[40] These wires are capable of conversion efficiencies in excess of 1E-4, into 75 keV to 100 keV continuum, with source sizes matching the wire diameter.[40] In the first implementation, the backlighting source will be produced by irradiating Au wires with the UV beams from two NIF quads, with a pulse duration of ~90 ps and energy of ~75 J/beam or ~600 J for the two quads. When the NIF Advanced Radiographic Capability (ARC) is available,[41] the 10 ps, 1 kJ/beam ARC pulses will be used to irradiate the Au micro-wires.

The main concerns for recording Compton radiographs of the fuel are related to the extreme background levels expected during the implosion. The plan for implementing the technique on the NIF attempts to take this into account, but experiments will be needed to validate the assumptions and modify the design if necessary. The radiographs will be recorded by the hardened hGXI that consists of a microchannel plate coupled to a framing camera, with gate times adjustable within the 30–200 ps range. This is calculated to mitigate the background associated with neutrons and gamma rays from the *n*-gamma induced reactions in the various components inside the NIF target chamber. A combination of collimators is predicted to reduce the background from hard x-rays generated by hot electrons traversing the hohlraum walls and from gamma rays from *n*-gamma induced reactions in nearby mass. Using a high-pass filter, coupled to the detector spectral response, we will limit the recorded x-ray photon energy to 60 –200 keV, to reduce the background from the x-rays emitted by the hot core. When fully implemented, the ARC backlighter will have four beams which can be timed and pointed independently. This should enable the use of multiple Au wires irradiated in a predefined temporal sequence, which should allow us to obtain multiple snapshots of the cold fuel around the time of peak compression. These radiographs will allow 2D reconstruction of the fuel density and shape.

The accuracy of measurements of fuel areal density depends mainly on the signal-to-noise ratio and on the contrast of the recorded radiograph. For the estimated background levels on NIF and the design described we expect signal-to-noise levels ~10–20. As stated above, this will need to be demonstrated in experiment. For these expected signal-to-noise levels we have estimated accuracies ~10% for measurements of limb-averaged ρR for implosions with

$\rho R \sim 1$ g/cm^2, when using short-pulse NIF UV beams to generate the backlighter, and about 2% when using NIF-ARC. Figure 18(a) shows a calculated 10 μm/70 ps, spatial/temporal resolution, Compton radiograph of a THD implosion. Figure 18(b) shows the same radiograph including the noise expected when using short-pulse NIF UV beams to generate the backlighter. Statistical Legendre analysis (50 realizations of the radiograph) along the limb contour shows peak fuel density a_n/a_0 shape accuracy of ~10% for $n=2$ and 4. The same analysis for the NIF-ARC option shows shape accuracies of ~3%.

VI. EXPERIMENTAL IGNITION THRESHOLD FACTOR

The THD diagnostics signatures described in Sec. IV can be used to confirm expectations from the experimental tuning campaign as well as to help identify areas that require further refinement in tuning. A simple example of this is possible refinement to the laser pulse shape or pointing to correct residual surrogacy errors in implosion symmetry carried over from gas filled CH capsule implosions used in the tuning campaign. In these implosions, unablated CH acts as a surrogate for the ice layer in a THD target. In simulations these surrogacy errors are ~10% in implosion shape and arise because the gas filled targets have lower convergence by $\sim \times 2$ and because the surrogate CH layer behaves slightly differently than the ice layer in THD targets. The THD observables are also used to predict DT performance. One way to do this would be to use the observables to relate back to the ITF formalism used for setting inputs in the tuning campaign. An alternate way is to use a combination of THD output performance variables to predict DT performance directly. These output variables can be cast in a form equivalent to a generalized Lawson criterion (GLC) for ICF[9,10] and is the subject of this section.

In order to investigate the relationship between THD and DT implosions, we have developed a numerical database of simulated implosions and associated x-ray and nuclear diagnostics outputs. This is composed of ~1000 sample points in the parameter space, each point constructed from four simulations: a 1D clean DT implosion, a 2D DT implosion, a 1D clean THD implosion, and a 2D THD implosion. The 1D clean calculations allow reference back to the ITF formalism which separates 1D and 3D phenomena. The input parameters to the implosions were selected to cover a range of ITF space that spans the predicted ignition cliff. Variations were included in target and laser parameters typical of those expected on a shot-to-shot basis, including amongst others drive asymmetry, ablator and ice roughness, laser pulse shape, and target thickness. A well tuned capsule is expected to have a high probability of ignition even when factoring in expected shot-to-shot variations. In order to span the ignition cliff the peak velocity, and fuel adiabat was allowed to span a larger range than expected shot-to-shot. The simulations typically include only the capsule. The simulations typically resolve modes up to ~30 which according to simulations is adequate for growth on the inside surface of the hot spot. This resolution is not adequate, however, to capture all of the ablation front growth which requires modes up to ~300. To account for higher mode growth and mixing at the interface between the ablator and ice, a mix model, chosen to match mass distribution profiles obtained from more highly resolved simulations,[42] was included.

A THD measurable parameter, ITFX $= (Y/Y_0)$ (dsf/0.07)$^{2.3}$ is found to be a good predictor of DT performance (see Fig. 19). Y is the measured neutron primary yield (defined as the integral between 13 and 15 MeV) and dsf is the measured down scattered fraction (defined as the number of neutrons between 10 and 12 MeV expressed as a fraction of those between 13 and 15 MeV). The precise limits on the energy range of the down scattered fraction are not found to be critical as long as the neutrons can be clearly distinguished from the TT neutrons. At ITFX = 1, as for ITF = 1, the probability of achieving gain = 1 is 50%, where gain is defined as the ratio of the energy produced by the burning capsule to the laser energy into the hohlraum. The constants

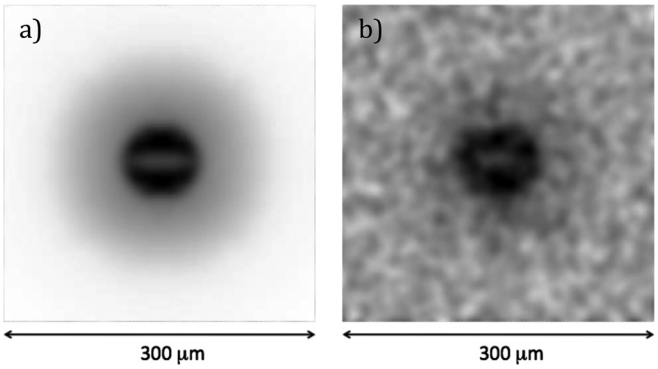

FIG. 18. (a) and (b) 10 μm/70 ps, spatial/temporal resolution, simulated Compton radiograph of a THD implosion: no noise (left) and with noise expected when using short-pulse NIF UV beams to generate the backlighter.

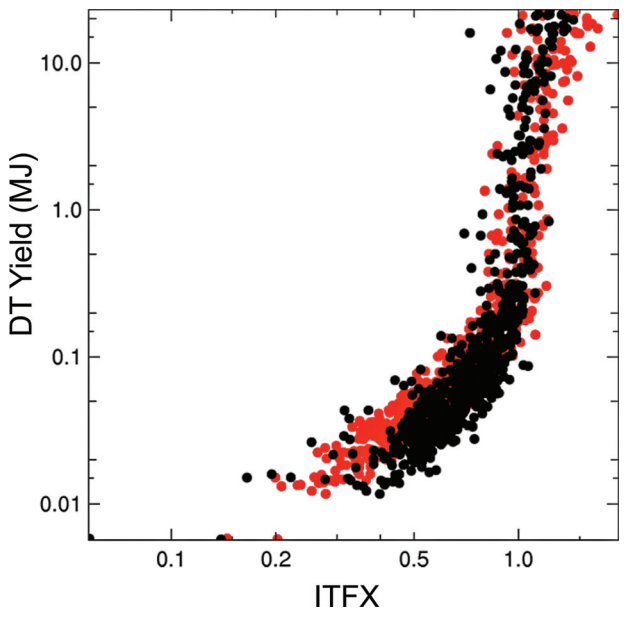

FIG. 19. (Color) Predictions of yield from simulated 2D DT implosions plotted against the observable performance metric, ITFX, ($Y \times$ dsf$^{2.3}$), (red dots) and the measurable Lawson criterion ($\rho R^2 \times T^{4.5} \times$ YOC) (black dots) from the equivalent THD implosions. The performance metric is normalized such that ITFX = 1 when $Y_{DT} = 1$ MJ. There are 1000 simulation pairs which include various combinations and degrees of off nominal specification to produce the performance variations seen. Both metrics order the DT data well.

in Experimental Ignition Threshold Factor (ITFX) above are the mean values for yield and dsf at G=1 for the 1.3 MJ CH capsule that is the baseline target for the first ignition campaign on NIF. The value for the yield depends on the D fraction and the number given, 1.8×10^{14}, is appropriate for 2% D. The dsf of 0.07 for neutrons between 10 and 12 MeV corresponds to a $\rho R\sim1.8$ g/cm^2. The motivation for ITFX derived both from the ITF formalism and the analysis of a generalized observable Lawson Criterion (GLC) in 1D (Ref. 9) and 3D (Ref. 10). The 3D GLC, which is equivalent to ITFX, can be written approximately as GLC $= (Y/Y_{1D})(T/3.0\text{keV})^{4.5}(\rho R/1.85\text{g/cm}^2.1.85\text{g/cm}^2)^2$. The second two terms capture the 1D implosion requirements while the first term is a measure of the degradation in performance of the hot spot as a result of 3D effects. The temperature dependence of the 1D yield for the THD implosions nearly cancels the temperature dependence of the temperature term in GLC so that IFTX requires only the yield and dsf. In the context of ITF, the mix and entropy terms in the ITF expression relate to ρR or equivalently dsf in ITFX, while velocity and shape in ITF relate to hot spot temperature and hot spot ρR, which in turn relate to yield Y in ITFX.

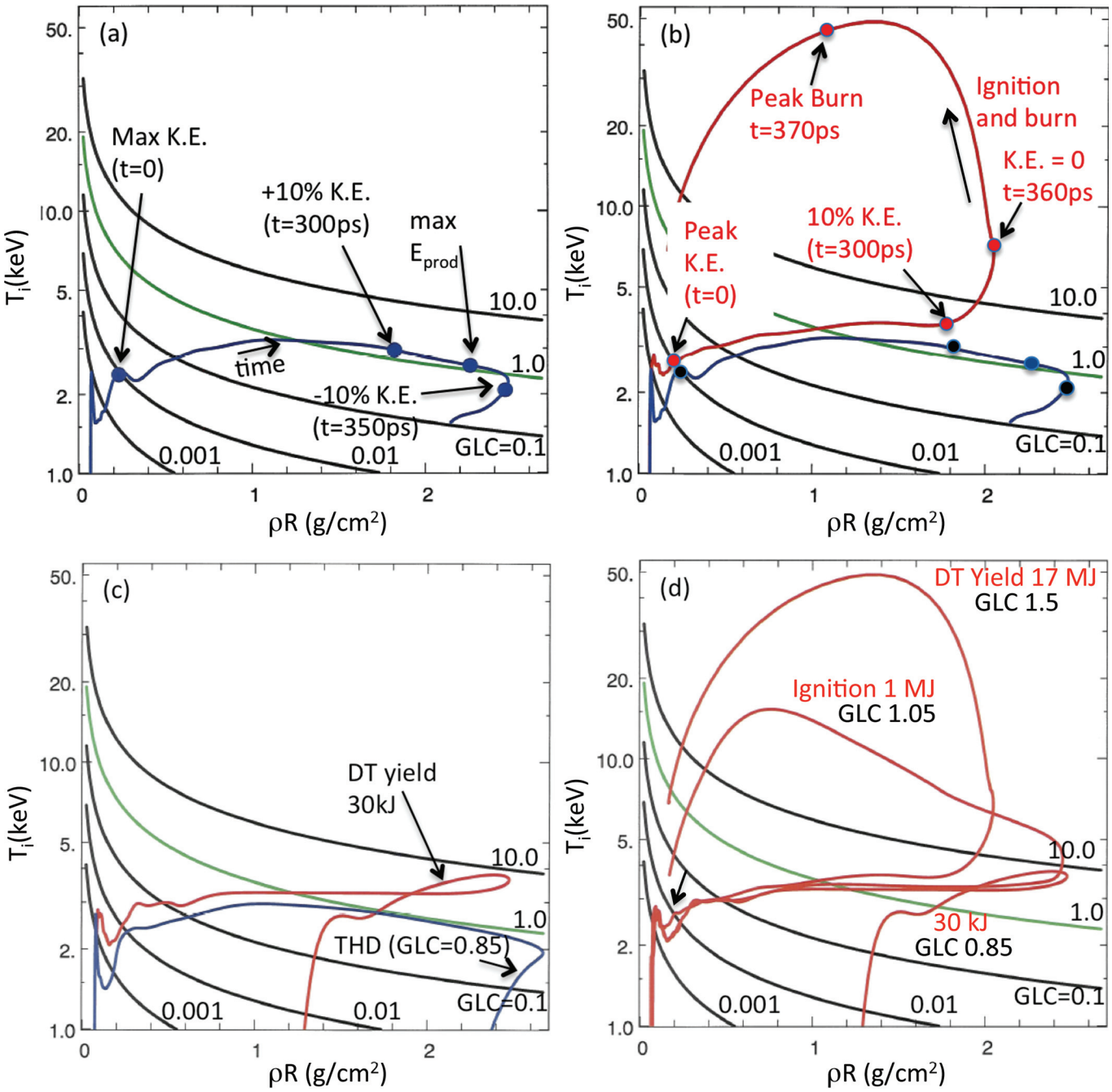

FIG. 20. (Color) Trajectories in T_{ion}–ρR space showing the threshold behavior of ignition near ITFX or GLC equal unity. Contours of ITFX (GLC) on all plots range from 10^{-3} to 10. (a) Trajectory of a THD capsule with GLC = 1.5 during the compression of the fuel starting at the time of peak kinetic energy. Points along the curve mark the time of peak kinetic energy, as well as 10% K.E., peak burn rate, and −10% K.E. (expansion). (b) The companion 50/50 implosion with ITF = 1.5 shows the rapid heating due to alpha particle deposition as the implosion approaches maximum compression. (c) The THD and equivalent DT implosion trajectories for an implosion with GLC = 0.85. Although there is some alpha heating, it is not rapid enough to heat the fuel to ignition conditions. (d) An implosion with a GLC = 1.05 has just enough alpha heating power to continue heating during the initial phases of expansion and reaches ignition conditions.

Figure 19 shows predicted yield from DT targets based on the THD performance metrics, ITFX, and the 3D measurable Lawson criterion from equivalent THD implosions. Both metrics order the data well and show the threshold behavior typical of ignition. Figure 19 shows that the ITFX or GLC required for ignition has some variability. Because ITFX, or GLC uses mass averaged quantities to characterize the state of the fuel, we find a ±15% uncertainty in the ITFX required for ignition in an ensemble of implosions in which the, laser, capsules are varied within specifications. There are also burn physics uncertainties which are not reflected in this plot but add an uncertainty in the location of the threshold. The main contributors to this are uncertainties in electron conduction and alpha particle range, each contributing approximately equally to a total uncertainty ~20–25% in the location of the ignition threshold. This is discussed further in Ref. 6.

Figure 20 shows the trajectories in the T_{ion}–ρR space for 1D implosions, one with an ITFX or GLC>1 and one with an ITFX or GLC<1. Also plotted are lines of constant GLC for the case in which the yield is assumed to equal the 1D yield. Any combination of temperature and ρR along those curves would have the same GLC. Figure 20(a) shows the trajectory in this space for an implosion with a GLC = 1.5. The trajectory plotted starts at the time of peak implosion velocity when the stagnation shock has collapsed to the center and raised the hot spot temperature to about 2 KeV. These are mass averaged quantities. Peak temperatures at the center of the hot spot are about twice these values. From this initial point, the kinetic energy in the imploding shell of fuel is gradually converted to internal energy over a period of about 300 ps. Points are shown along the implosion trajectory when 10% of the kinetic energy remains at peak energy production and at a time when the shell is expanding and again has 10% of its initial kinetic energy. It is interesting to note that the implosion follows a contour of nearly constant GLC as it approaches peak compression. Plotted in Fig. 20(b) is the companion implosion for a 50/50 DT fuel implosion. It parallels the THD implosion until alpha heating is large enough to cause a rapid heating of the fuel. One feature evident in Fig. 20(b) is the slight offset in the temperatures of the THD and DT trajectories throughout the early phase of the implosion. This arises because of the disparity in the composition of the central gas and cryo-layer in the THD implosion as described above. Because of this, in the THD targets we are not able to match both the mass and particle density of the DT implosions.

Figure 20(c) shows similar trajectories for a capsule with a GLC = 0.85. There is some alpha heating in the DT target but the heating is insufficient to raise the fuel temperature to ignition conditions before it starts cooling from expansion. This implosion has a yield of only 30 kJ. Figure 20(d) shows the trajectory for an implosion with a GLC = 1.05, just above the ignition threshold. This implosion has a yield of 1 MJ and the alpha heating is just sufficient to continue heating at the capsule begins expanding.

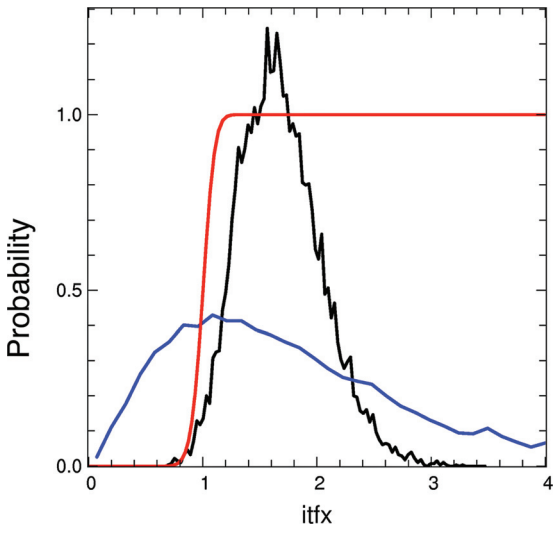

FIG. 21. (Color) Probability of ignition ($Y > 1$ MJ) (red) constructed from the numerical database shown in Fig. 19. Also shown are the expected DT experiment distribution (black) after the tuning campaign and how this distribution is distorted by measurement error of ±10% in each of Y and dsf (blue). Multiple shots should help narrow the latter towards the true distribution.

TABLE III. Expected THD implosion observables predicted by a large suite of hydra simulations for experiments meeting point design specifications[6] after a successful tuning campaign in which the laser pulse and target parameters have been adjusted to meet the point design specifications.[7]

Observable	Average value	RMS	RMS/AVG
Y_n (13–15 MeV)	2.0×10^{14}	0.37×10^{14}	0.19
dsf n(10–12)/n(13–15)	0.078	0.0044	0.06
T_{ion} (keV)	3.52	0.14	0.04
R_{HS} (μm)	30	2.5	0.08

Y_n (13–15 MeV): number of neutrons with energies between 13 and 15 MeV escaping the capsule.
dsf: ratio of number of neutrons escaping the capsule with energies between 10 and 12 MeV to those with energies between 13 and 15 MeV. This is a measure of the average ρR of the assembled fuel and ablator ($\rho R_{TOT} \sim 28$dsf g/cm^2).
T_{ion}: burn averaged ion temperature as inferred from the width of the spectrum of DT neutrons emerging from the capsule.[11]
R_{HS}: hot spot radius at peak x-ray emission.

A. THD performance and ITFX

The THD performance metrics will be measured by the diagnostics mentioned in Sec. IV and will be used to predict the probability of ignition. Assessing the probability of ignition is complicated by two principal factors.

First, the expected experimental output for an ensemble of shots is distributed in ITFX space approximately log-normally due to shot-to-shot laser and target variations as shown in Fig 21. The ITFX distribution shown has been constructed from the 2D simulation data base, assuming the laser, targets and tuning experiments have met requirements.[6,7] The width of the distribution is ~ ±30%, of which most (~20% vs 30%) is due to variations in Y. Table III tabulates the expected variability in some of the more important implosion characteristics for an experimental system that meets the point design specification set out in Ref. 6.

Second, experimental measurement uncertainties must also be considered in addition to intrinsic shot-to-shot variations. If the measurement error in ITFX is σ_{ITFX}, and the

width of the experimental system is σ_{exp}, the estimate of the accuracy in the mean value of ITFX from n shots is approximately $\sqrt{(\sigma_{ITFX}^2 + \sigma_{exp}^2)n}$. For example, if each of dsf and Y are measured to $\pm 10\%$, i.e., each measurement of ITFX is made to $\sim \pm 20\%$ and the width of the ITFX distribution is $\sim \pm 30\%$, the error in the mean ITFX is only $\sim 35\%$ and dominated by shot-to-shot variability. Several shots would be required to start to provide confidence in these estimates and in the system performance. For example, with $\pm 10\%$ diagnostics errors in Y and dsf, three repeat shots would provide a mean value of ITFX to $\sim \pm 20\%$ and would indicate whether the estimates of shot-to-shot variability were reasonable. Because the expected value of ITFX for the current CH point design at $\sim$1.3 MJ, after the experimental tuning campaign, is 1.5 (Ref. 6) the estimate in the error in the measured three shot average would be $\sim \pm 0.3$.

Finally, to minimize potential surrogacy errors between our calculated THD performance and the equivalent DT performance, we can use 50/50 DT shots to calibrate the ITFX metric as the quality of imploded fuel is optimized. Prior to the tuning experiments, the ITFX value would be expected to be $\ll 1$. As improvements are made to the laser pulse shape, equivalent improvements should be seen in ITFX and in the yield of DT targets, both of which could be measured. This will enable adjustment of predictive tools as the campaign progresses.

VII. CONCLUSION

Dudded fuel (THD) layered implosions are good surrogates of DT implosions until α-heating begins in the hot spot formation phase once $<T_{HS}>\sim$ 3keV. The THD's can be used to check and adjust parameters set during the experimental tuning campaign as well as to predict the performance of equivalent DT targets. A large 2D simulation data base has been used to investigate performance metrics and a good predictor of DT performance has been found to be $\mathrm{ITFX} = Y\mathrm{dsf}^{2.3}$, which has been shown to be equivalent to a generalized measurable Lawson criterion for ICF.[9,10] A variety of diagnostics will be used to measure x-ray and nuclear information to provide this and other complementary information about the THD and DT implosions.

ACKNOWLEDGEMENT

This work was performed under the auspices of the U.S. Department of Energy by Lawrence Livermore National Laboratory under Contract No. DE-AC52-07NA27344.

[1]E. I. Moses, J. Phys.: Conf. Ser. **112**, 012003 (2008).
[2]G. H. Miller, E. I. Moses, and C. R. Wuest, Nucl. Fusion **44**, 228 (2004).
[3]J. Nuckols, L. Wood, A. Thiessen, and G. Zimmerman, Nature **239**, 139 (1972).
[4]J. D. Lindl, Phys. Plasmas **2**, 3933 (1995);J. D. Lindl Lindl, P. Amendt, R. L. Berger, S. G. Glendinning, S. H. Glenzer, S. W. Haan, R. L. Kauffman, O. L. Landen, and L. J. Suter, Phys. Plasmas **11**, 339 (2004).
[5]S. Atzeni and J. Meyer-Ter-Vehn, *The Physics of Inertial Fusion* Oxford Science Publications, Clarendon, Oxford, 2004.
[6]S. W. Haan, J. D. Lindl, D. A. Callahan, D. S. Clark, J. D. Salmonson, B. A. Hammel, L. J. Atherton, R. C. Cook, M. J. Edwards, S. Glenzer, A. V. Hamza, S. P. Hatchett, M. C. Herrmann, D. E. Hinkel, D. D. Ho, H. Huang, O. S. Jones, J. Kline, G. Kyrala, O. L. Landen, B. J. MacGowan, M. M. Marinak, D. D. Meyerhofer, J. L. Milovich, K. A. Moreno, E. I. Moses, D. H. Munro, A. Nikroo, R. E. Olson, K. Peterson, S. M. Pollaine, J. E. Ralph, H. F. Robey, B. K. Spears, P. T. Springer, L. J. Suter, C. A. Thomas, R. P. Town, R. Vesey, S. V. Weber, H. L. Wilkens, and D. C Wilson, Phys. Plasmas **18**, 051001 (2011).
[7]O. L. Landen, J. Edwards, S. W. Haan, H. F. Robey, J. Milovich, B. K. Spears, S. V. Weber, D. S. Clark, J. D. Lindl, B. J. MacGowan, E. I. Moses, J. Atherton, P. A. Amendt, T. R. Boehly, D. K. Bradley, D. G. Braun, D. A. Callahan, P. M. Celliers, G. W. Collins, E. L. Dewald, L. Divol, J. A. Frenje, S. H. Glenzer, A. Hamza, B. A. Hammel, D. G. Hicks, N. Hoffman, N. Izumi, O. S. Jones, J. D. Kilkenny, R. K. Kirkwood, J. L. Kline, G. A. Kyrala, M. M. Marinak, N. Meezan, D. D. Meyerhofer, P. Michel, D. H. Munro, R. E. Olson, A. Nikroo, S. P. Regan, L. J. Suter, C. A. Thomas, and D. C. Wilson, Phys. Plasmas **18**, 051002 (2011).
[8]B. K. Spears, S. Brandon, D. Clark, C. Cerjan, J. Edwards, O. Landen, J. Lindl, S. Haan, S. Hatchett, J. Salmonson, P. Springer, S. Weber, D. Wilson, J. Phys.: Conf. Ser. **244**, 022014 (2010).
[9]C. D. Zhou and R. Betti, Phys. Plasmas **15**, 102707 (2008).
[10]P. Chang, R. Betti, B. K. Spears, K. S. Anderson, J. Edwards, M. Fatenejad, J. D. Lindl, R. L. McCrory, R. Nora, and D. Shvarts, Phys. Rev. Lett. **104**, 135002 (2010); R. Betti, P. Y. Chang, B. K. Spears, K. S. Anderson, J. Edwards, M. Fatenejad, J. D. Lindl, R. L. McCrory, R. Nora, and D. Shvarts, Phys. Plasmas **17**, 058102 (2010).
[11]H. Brysk, Plasma Phys. **15**, 611 (1973).
[12]T. J. Murphy, J. M. Wallace, N. D. Delamater, C. W. Barnes, P. Gobby, A. A. Hauer, E. Lindman, G. Magelssen, J. B. Moore, J. A. Oertel, R. Watt, O. L. Landen, P. Amendt, M. Cable, C. Decker, B. A. Hammel, J. A. Koch, L. J. Suter, R. E. Turner, R. J. Wallace, F. J. Marshall, D. Bradley, R. S. Craxton, J. P. Knauer, R. Kremens, and J. D. Schnittman, Phys. Rev. Lett. **81**, 108 (1998); R. E. Turner, P. Amendt, O. L. Landen *et al.*, Phys. Plasmas **7**, 333 (2000); R. E. Turner, P. A. Amendt, O. L. Landen, L. J. Suter, R. J. Wallace, and B. A. Hammel, Phys. Plasmas **10**, 2429 (2003); P. A. Amendt, R. E. Turner, and O. L. Landen, Phys. Rev. Lett. **89**, 165001 (2002); G. Kyrala, A Seifter, J. Kline, N. Hoffman, S. R. Goldman, BAPS **53**, 330 (2008); P. Michel, L. Divol, E. A. Williams, S. Weber, C. A. Thomas, D. A. Callahan, S. W. Haan, J. D. Salmonson, S. Dixit, D. E. Hinkel, M. J. Edwards, B. J. MacGowan, J. D. Lindl, S. H. Glenzer, and L. J. Suter, Phys. Rev. Lett. **102**, 025004 (2009).
[13]J. L. Atherton, J. Phys. Conf. Ser. **112**, 032063 (2008).
[14]A. Nikroo, K. C. Chen, M. L. Hoppe, H. Huang, J. R. Wall, H. Xu, M. W. McElfresh, C. S. Alford, R. C. Cook, J. C. Cooley, R. Fields, R. Hackenberg, R. P. Doerner, and M. Baldwin, Phys. Plasmas **13**, 056302 (2006); K. C. Chen, R. C. Cook, H. Huang, S. A. Letts, and A. Nikroo, Fusion Sci. Technol. **49**, 750 (2006).
[15]T. C. Sangster, R. Betti, R. S. Craxton, J. A. Delettrez, D. H. Edgell, L. M. Elasky, V. Yu. Glebov, V. N. Goncharov, D. R. Harding, D. Jacobs-Perkins, R. Janezic, R. L. Keck, J. P. Knauer, S. J. Loucks, L. D. Lund, F. J. Marshall, R. L. McCrory, P. W. McKenty, D. D. Meyerhofer, P. B. Radha, S. P. Regan, W. Seka, W. T. Shmayda, S. Skupsky, J. A. Frenje, C. K. Li, R. D. Petrasso, F. H. Sequin, J. D. Moody, J. A. Atherton, B. D. MacGowan, J. D. Kilkenny, T. P. Bernat, and D. S. Montgomery, Phys. Plasmas **14**, 058101 (2007).
[16]P. C. Souers, *Hydrogen Properties for Fusion Energy* University of California, Berkeley, 1986.
[17]D. S. Clark, S. W. Haan, B. A. Hammel, J. D. Salmonson, D. A. Callahan, and R. P. J. Town, Phys. Plasmas **17**, 1 (2010).
[18]S. W. Haan, M. C. Herrmann, T. R. Dittrich, A. J. Fetterman, M. M. Marinak, D. H. Munro, S. M. Pollaine, J. D. Salmonson, G. L. Strobel, and L. J. Suter, Phys. Plasmas **12**, 056316 (2005).
[19]E. L. Dewald, M. Rosen, S. H. Glenzer, L. J. Suter, F. Girard, J. P. Jadaud, J. Schein, C. Constantin, F. Wagon, G. Huser, P. Neumayer, and O. L. Landen, Phys. Plasmas **15**, 072706 (2008).
[20]S. W. Haan, D. A. Callahan, M. J. Edwards, B. A. Hammel, D. D. Ho, O. S. Jones, J. D. Lindl, B. J. MacGowan, M. M. Marinak, D. H. Munro, S. M. Pollaine, J. D. Salmonson, B. K. Spears, and L. J. Suter, Fusion Sci. Technol. **55**, 227 (2009).
[21]R. Kishony and D. Shvarts, Phys. Plasmas **8**, 4925 (2001).
[22]B. A. Hammel, M. J. Edwards, S. W. Haan, M. M. Marinak, M. Patel, H. Robey, and J. Salmonson, J. Phys.: Conf. Ser. **112**, 022007 (2008).
[23]M. M. Marinak, G. D. Kerbel, N. A. Gentile, O. Jones, D. Munro, S. Pollaine, T. R. Dittrich, and S. W. Haan, Phys. Plasmas **8**, 2275 (2001);G. B. Zimmerman and W. L. Kruer, Comments Plasma Phys. Controlled Fusion **2**, 51 (1975).
[24]R. P. J. Town, M. D. Rosen, P. A. Michel, L. Divol, J. D. Moody, G. A. Kyrala, M. B. Schneider, J. L. Kline, C. A. Thomas, J. L. Milovich, D. A.

Callahan, N. B. Meezan, D. E. Hinkel, E. A. Williams, R. L. Berger, M. J. Edwards, L. J. Suter, S. W. Haan, J. D. Lindl, E. L. Dewald, S. Dixit, S. H. Glenzer, O. L. Landen, E. I. Moses, H. A. Scott, J. A. Harte, and G. B. Zimmerman, Phys. Plasmas **18**, 056302 (2011).
[25]C. A. Iglesias and F. J. Rogers, Astrophys. J. **464**, 943 (1996).
[26]M. H. Chen, private communication;C. A. Iglesias and B. G. Wilson, J. Quant. Spectrosc. Radiat. Transf. **52**, 127 (1994).
[27]D. A. Young and E. M. Corey, J. Appl. Phys. **78**(6), 3748 (1995).
[28]J. A. Oertel, R. Aragonez, T. Archuleta, C. Barnes, L. Casper, V. Fatherley, T. Heindrichs, R. King, D. Landers, F. Lopez, P. Sanchez, G. Sandoval, L. Schrank, P. Walsh, P. Bell, M. Brown, R. Costa, J. Holder, S. Montelongo, and N. Pederson, Rev. Sci. Instrum. **77**(10), 10E308 (2006).
[29]N Izumi, G. Stone, C. Hagmann, C. Sorce, D. K. Bradley, M. Moran, O. L. Landen, P. Springer, W. Stoeffl, R. Tommasini, H. W. Hermann, G. A. Kyrala, V. Y. Glebov, J Knauer, T. C. Sangster, and J. A. Koch, J. Phys.: Conf. Ser. **244**, 032048 (2010).
[30]J. A. Koch, S. W. Haan, and R. C. Mancini, J. Quant. Spectrosc. **88**, 433 (2004).
[31]E. Loomis, G. Grim, C. Wilde, D. C. Wilson, M. Wilke, J. Finch, G. Morgan, I. Tregillis, D. Clark, J. Phys.: Conf. Ser. **244**, (2010) 032051.
[32]D. C. Wilson, W. C. Mead, L. Disdier, M. Houry, J.-L. Bourgade, and T. J. Murphy, Nucl. Instrum. Methods A **488**(1), 400 (2002).
[33]Z. A. Ali, V. Y. Glebov, M. Cruz, T. Duffy, C. Stoeckl, S. Roberts, T. C. Sangster, R. Tommasini, A. Throop, M. Moran, L. Dauffy, and C. Horsefield Rev. Sci. Instrum. **79**, 10E527 (2008); V. Y. Glebov, D. D. Meyerhofer, T. C. Sangster, C. Stoeckl, S. Roberts, C. A. Barrera, J. R. Celeste, C. J. Cerjan, L. S. Fauffy, D. C. Eder, R. L. Griffith, S. W. Haan, B. A. Hammel, S. P. Hatchett, N. Izumi, J. R. Kimbrough, J. A. Koch, O. L. Landen, R. A. Lerche, B. J. MacGowan, M. J. Moran, E. W. Ng, T. W. Phillips, P. M. Song, R. Tommasini, B. K. Young, S. E. Caldwell, G. P. Grim, S. C. Evans, J. M. Mack, T. J. Sedillo, M. D. Wilke, D. Casey, J. A. Frenje, C. K. Li, R. D. Petrasso, F. H. Sequin, J. L. Bourgade, L. Disdier, M. Houry, I. Lantuejoul, O. Landoas, G. A. Chandler, G. W. Cooper, R. J. Leeper, R. E. Olson, C. L. Ruiz, M. A. Sweeney, S. P. Padalino, C. Horsfield, B. A. Davis, Rev. Sci. Instrum. **77**, 10E715 (2006); V. Y. Glebov, C. Stoeckl, T. C. Sangster, S. Roberts, R. A. Lerche, G. J. Schmid, IEEE Trans. Plasma Sci. **33**, 70 (2005); V. Y. Glebov, C. Stoeckl, T. C. Sangster, S. Roberts, G. J. Schmid, R. A. Lerche, and M. J. Moran, Rev. Sci. Instrum. **75**, 3559 (2004); G. J. Schmid, R. L. Griffith, N. Izumi, J. A. Koch, R. A. Lerche, M. J. Moran, T. W. Phillips, R. E. Turner, V. Y. Glebov, T. C. Sangster, and C. Stoeckl, Rev. Sci. Instrum. **74**, 1828 (2003).
[34]J. A. Frenje, D. T. Casey, C. K. Li, F. H. Seguin, R. D. Petrasso, V. Y. Glebov, P.B. Radha, T. C. Sangster, D. D. Meyerhofer, S. P. Hatchett, S. W. Haan, C. J. Cerjan, O. L. Landen, K. A. Fletcher, and R. J. Leeper, "Probing high areal-density cryogenic deuterium-tritium implosions using downscattered neutron spectra measured by the magnetic recoil spectrometer" (AIP, Melville, NY, 2010), No. 5, p. 056311.
[35]B. Singh, Nucl. Data Sheets **85**, 1 (1998) 101; H. Junde, Nucl. Data Sheets **91**, (2000) 366.
[36]H. W. Herrmann, C. S. Young, J. M. Mack, Y. H. Kim, A. McEvoy, S. Evans, T. Sedillo, S. Batha, M. Schmitt, D. C. Wilson, J. R. Langenbrunner, R. Malone, M. I. Kaufman, B. C. Cox, B. Frogger, E. K. Miller, Z. A. Ali, T. W. Tunnell, W. Stoeffl, C. J. Horsfield, and M. Rubery, J. Phys.: Conf. Ser. **244**, 032047 (2010).
[37]D. C. Wilson, P. A. Bradley, H. W. Herrmann, B. K. Spears, C. J. Cerjan, J. D. Salmonson, S. P. Hatchett II, and V. Yu. Glebov, Rev. Sci. Instrum. **79**, 10E502 (2008)
[38]R. Tommasini, H. S. Park, P. Patel, B. Maddox, S. Le Pape, S. P. Hatchett, B. A. Remington, M. H. Key, N. Izumi, M. Tabak, J. A. Koch, O. L. Landen, D. Hey, A. MacKinnon, J. Seely, G. Holland, L. Hudson, C. Szabo, *AIP Conf. Proc. 15th International Conference on Atomic Processes in Plasmas* (Gaithersburg, 2007), p. 248.
[39]R. Tommasini, A. MacPhee, D. Hey, T. Ma, C. Chen, N. Izumi, W. Unites, A. MacKinnon, S. P. Hatchett, B. S. Remington, H. S. Park, P. Springer, J. A. Koch, O. L. Landen, J. Seeley, G, Holland, and L. Hudson, Rev. Sci. Instrum. **79**, 10E901 (2008).
[40]R. Tommasini, S. Hatchett, D. Hey, C. Iglesias, N. Izumi, O. L. Landen, A. J. MacKinnon, C. Sorce, J. A. Delettrez, V. Yu Glebov, J. C. Sangster, and C. Stoekl, Phys. Plasmas **18**, 056309 (2011).
[41]C. P. J. Barty, M. Key, J. Britten, R. Beach, G. Beer, C. Brown, S. Bryan, J. Caird, T. Carlson, J. Crane, J. Dawson, A. C. Erlandson, D. Fittinghoff, M. Hermann, C. Hoaglan, A. Iyer, L. Jones II, I. Jovanovic, A. Komashko, O. Landen, Z. Liao, W. Molander, S. Mitchell, E. Moses, N. Nielsen, H-H. Nguyen, J. Nissen, S. Payne, D. Penington, L. Risinger, M. Rushford, K. Skulina, M. Spaeth, B. Stuart, G. Tietbohl, and B. Wattellier, Nucl. Fusion **44**(12), S266 (2004).
[42]B. A. Hammel, S. W. Haan, D. S. Clark, M. J. Edwards, S. H. Langer, M. M. Marinak, M. V. Patel, J. D. Salmonson, H. A. Scott, High Energy Density Phys. **6**(2), 171 (2010).